https://doi.org/10.5194/gmd-2023-231
Preprint. Discussion started: 10 January 2024


Geoscientific Model Development Discussions
Open Access

# Implementation of a brittle sea-ice rheology in an Eulerian, finite-difference, C-grid modeling framework: Impact on the simulated deformation of sea-ice in the Arctic

Laurent Brodeau[1], Pierre Rampal[1], Einar Ólason[2], and Véronique Dansereau[3]
[1]IGE/CNRS, Grenoble, France.
[2]NERSC, Bergen, Norway.
[3]ISTERRE/CNRS, Grenoble, France.
**Correspondence:** Laurent Brodeau (laurent.brodeau@univ-grenoble-alpes.fr)

**Abstract.** We have implemented the Brittle Bingham-Maxwell sea-ice rheology (BBM) into SI3, the sea-ice component of NEMO. We describe how we achieved this numerical implementation. Specifically, we detail how we introduced a new spatial discretization framework, well adapted to solve the equations of sea-ice dynamics, in order to overcome the numerical issues posed by the use of the staggered C-grid. As a validation step, a twin hindcast experiment performed with the coupled ocean/sea-ice setup of the NEMO system, run at a 1/4°spatial resolution, serves as a basis to evaluate the simulated sea-ice deformation rates against satellite observations; when using the newly-implemented BBM rheology and when using the default viscous-plastic rheology of SI3. The results show the added value of using a brittle-type of rheology, such as BBM, to accurately simulate the highly-localized deformation patterns of sea-ice. Thus, our results highlight the relevance of the use of this newly-implemented rheology for future modeling studies that utilize a classical *Eulerian* sea-ice modeling framework, *i.e.* based on the finite-difference discretization method over a quadrilateral, staggered, computational grid. This includes, in particular, coupled climate simulations performed with CMIP-class Earth System Models at coarse to moderate spatial resolution.

## 1 Introduction

Sea-ice is one of the most important physical interfaces in the climate system, as it directly impacts the ocean and the atmosphere, at both local and global scales (Vihma, 2014; IPCC, 2022). In polar regions, the sea-ice cover indeed modulates all the radiative and turbulent exchanges of heat, freshwater, gas, and momentum, between the ocean and the atmosphere (*e.g.* Taylor et al., 2018, for a review). At the local scale, these fluxes strongly depend on the heterogeneity of the sea-ice thickness, which itself is controlled by the sea-ice dynamics and the associated formation of leads and ridges. This makes the representation of sea-ice dynamics key when seeking to simulate the coupled, multi-component earth system, both in the context of regional or global climate simulations, or in the context of short-term sea-ice predictions.

The dynamical behavior of sea-ice is controlled by processes interacting and evolving over a wide range of spatial and temporal scales. This multi-scale nature of sea-ice physics is fascinating and has triggered the curiosity of geophysicists since

https://doi.org/10.5194/gmd-2023-231
Preprint. Discussion started: 10 January 2024

Geoscientific Model Development Discussions

the early 70's (Coon et al., 1974). More recently, scientific interest in sea-ice dynamics has grown significantly due to the dramatic retreat and thinning of the Arctic sea-ice cover. In addition, the abundance of new observations of sea-ice kinematics, recorded by both *in-situ* instruments and satellites, greatly enhances the potential for further development in sea-ice modeling.

The dynamics of sea-ice is undoubtedly complex. As one highlight of this complexity, Rampal et al. (2008); Weiss et al. (2009) showed that the statistical properties of sea-ice deformation are characterized by a coupled space-time multifractal scaling invariance, similar to what is observed for the deformation of the Earth's crust (Kagan and Jackson, 1991; Marsan and Weiss, 2010). The spatial and temporal scaling properties of sea-ice deformation and their coupling provide evidence for the strong heterogeneity and intermittency that characterizes sea-ice dynamics (Rampal et al., 2008).

Attempting to reproduce the discontinuous nature of sea-ice – related to the presence of fractures and leads – in continuous sea-ice models, as well as the complexity of the spatial patterns and temporal evolution of these features, poses a fundamental and major challenge (*e.g.* Bouchat et al., 2022; Hutter et al., 2022).

Following the work of Girard et al. (2011), who pioneered the use of an elasto-brittle rheology based on the concept of material damage in the context of sea-ice modeling, the Maxwell-Elasto-Brittle rheology (hereafter MEB) was developed to tackle this challenge (Dansereau et al., 2016). It was implemented into neXtSIM – a large-scale dynamical-thermodynamical Lagrangian finite element sea-ice model (Rampal et al., 2016) – to evaluate the performance of this new rheology in a realistic simulation of the Pan-Arctic region. The sea-ice deformations simulated by neXtSIM over a winter season have been first evaluated statistically against satellite observations, in terms of PDFs and scaling invariance properties, in Rampal et al. (2016) and Rampal et al. (2019), and later in the two companion papers of Bouchat et al. (2022) and Hutter et al. (2022), showing satisfying results.

Recently, the Brittle Bingham Maxwell rheology (hereafter BBM), has been proposed by Ólason et al. (2022) as an upgrade of MEB. One of the main motive behind the development of BBM was to make realistic multidecadal sea-ice simulations possible, while preserving (i) the scaling properties of sea-ice deformation from the model grid cell up to the scale of the Arctic basin, and (ii) the thickness pattern of the sea-ice cover consistent with observations (Ólason et al., 2022; Boutin et al., 2023). These two constraints have proved to be impossible to respect with MEB because of an incomplete treatment of the convergence of highly damaged sea-ice, which results in unrealistic sea-ice thicknesses after a couple of years of model integration.

MEB and BBM have been successfully implemented and tested in neXtSIM. Yet, using neXtSIM in the context of coupled simulations (such as ocean/sea-ice) is challenging because: (i) the pure *Lagrangian* advection scheme on which neXtSIM is built implies that a *Lagrangian-Eulerian* coupler has to be used, and (ii) its weak scalability capabilities when run in parallel on more than a few processors makes it a bottleneck for the coupled setup.

The implementation of BBM into an existing and widely-used state-of-the-art sea-ice model, such as SI3, has the potential to significantly benefit the sea-ice, ocean, and climate modeling communities. First, this allows to compare the brittle and non-brittle rheologies in a modeling framework that these communities are familiar with. Second, it makes the assessment of the impact of these rheology-driven differences in coupled modeling systems easily achievable, and simulations at the kilometer-scale possible thanks to the excellent scalability capabilities of SI3 (parallel computing). And third, it facilitates the adoption of this type of brittle sea-ice rheology, making it accessible to a broader community of modelers.

https://doi.org/10.5194/gmd-2023-231
Preprint. Discussion started: 10 January 2024




As far as we know, a few attempts have been made to implement MEB in *Eulerian* sea-ice models that utilize the finite-difference discretization method on staggered grids, such as the MIT general circulation model, or LIM, the former sea-ice component of the NEMO modeling system (Rousset et al., 2015)). Recently, Plante et al. (2020) presented an implementation of MEB in the McGill sea-ice model (Tremblay and Mysak, 1997; Lemieux et al., 2008, 2014). In their study, the simulations use an idealized configuration (ice flowing through a narrowing channel) over a short period of time (10 hours), and the contribution of terms related to the horizontal advection is not considered. The idealized nature of these simulations prevented their results from being assessed against observations of sea-ice drift and deformation.

Overall, the efforts of these modeling groups have demonstrated the challenge inherent to the implementation of brittle rheologies in realistic *Eulerian* models that use the finite-difference method on staggered grids. Indeed, as pointed out by Plante et al. (2020), one major problem linked to the use of the C-grid is the fact that the discretized components of the strain-rate and internal stress tensors are staggered in space; with the trace (normal) components being defined at the center of the cell, and the shearing components at the corners. As it is going to be extensively discussed in the present study, the resort to spatial interpolation to overcome this problem, as currently done in VP implementations, is not well-suited for brittle rheologies. Therefore, this problem needs to be addressed in order for these *Eulerian* finite-difference/C-grid-based sea-ice models to be able to simulate the deformation of sea-ice with a level or realism similar to that obtained with *e.g.* neXtSIM (Rampal et al., 2019; Ólason et al., 2022; Boutin et al., 2023).

In this paper, we propose a solution to this problem and provide a detailed description of the implementation of BBM into an *Eulerian*, finite-difference, staggered-grid modeling framework; namely that of SI3, the sea-ice component of the NEMO modeling system. As a validation procedure, we then compare the simulated sea-ice deformations obtained with our BBM SI3 implementation against those constructed from satellite observations. These deformations are also compared to those obtained with the default viscous-plastic rheology of SI3 (*i.e.* the aEVP rheology of Kimmritz et al., 2016).

This paper is organized as follows. In section 2, we summarize the equations of the sea-ice dynamics model, discuss the aspects in which the numerical implementation of a brittle rheology may differ from that of a viscous-plastic one, and detail the numerical aspects of our implementation of BBM into SI3. In section 3, we describe the NEMO ocean/sea-ice coupled setup used to perform our simulations with both the newly-implemented BBM and the default viscous-plastic rheology, and how these simulations are designed, before focusing on the evaluation the simulated sea-ice deformations. In section 4, we discuss some important aspects of our study, linked to both the numerical implementation and the simulated sea-ice deformations. Our conclusions are summarized in section 5.

A detailed nomenclature relating the acronyms and symbols used throughout the paper is outlined in Appendix A.

https://doi.org/10.5194/gmd-2023-231
Preprint. Discussion started: 10 January 2024

Geoscientific Model Development
Discussions

## 2 Model and implementation

### 2.1 Governing equations and constitutive law

The two-dimensional, vertically-integrated, momentum equation for sea-ice reads

$$m\,\partial_t \vec{u} = \vec{\nabla}\cdot\left(h\boldsymbol{\sigma}\right) + A\left(\vec{\tau}_a + \vec{\tau}\right) + m f\,\vec{k}\times\vec{u} - m g \vec{\nabla} H, \tag{1}$$

where the variables and symbols are all defined in Appendix A1. In the two-dimensional (plane stresses) case, the stress tensor writes

$$\boldsymbol{\sigma} = \begin{pmatrix} \sigma_{11} & \sigma_{12} \\ \sigma_{12} & \sigma_{22} \end{pmatrix}. \tag{2}$$

In general, a constitutive law relates $\boldsymbol{\sigma}$ to the strain-rate tensor $\dot{\boldsymbol{\varepsilon}}$, defined as follows:

$$\dot{\boldsymbol{\varepsilon}} = \begin{pmatrix} \dot{\varepsilon}_{11} & \dot{\varepsilon}_{12} \\ \dot{\varepsilon}_{12} & \dot{\varepsilon}_{22} \end{pmatrix} \equiv \begin{pmatrix} \partial_x u & \frac{1}{2}(\partial_y u + \partial_x v) \\ \frac{1}{2}(\partial_y u + \partial_x v) & \partial_y v \end{pmatrix}. \tag{3}$$

As derived by Ólason et al. (2022) (their Eq. 20), the BBM constitutive equation reads

$$\partial_t \underline{\boldsymbol{\sigma}} = E\,\boldsymbol{K}\cdot\underline{\dot{\boldsymbol{\varepsilon}}} - \underline{\boldsymbol{\sigma}}\frac{1}{\lambda}\left(1 + \tilde{P} + \frac{\lambda}{1-d}\,\partial_t d\right), \tag{4}$$

where the underbar notation indicates that the tensors are expressed in their pseudovector form, and $\boldsymbol{K}$ is the elastic stiffness tensor:

$$\boldsymbol{K} = \frac{1}{1-\nu^2}\begin{pmatrix} 1 & \nu & 0 \\ \nu & 1 & 0 \\ 0 & 0 & 1-\nu \end{pmatrix}. \tag{5}$$

In equation 4, $d$ is the damage scalar: a variable that represents the density of fractures in the ice at the subgrid-scale. In a way similar to that of the sea-ice concentration, $A$, the damage modulates the elastic modulus and apparent viscous relaxation time of the ice as

$$E = E_0(1-d)\,e^{-C(1-A)}, \tag{6}$$

$$\lambda = \lambda_0\left[(1-d)e^{-C(1-A)}\right]^{\alpha-1}, \tag{7}$$

where $C$ is the compaction parameter constant and $\alpha$ is a constant exponent greater than 1. $\alpha$ fulfills the physical constraint that the relaxation time for the stress also decreases as damage increases, and re-increases as the ice heals (*i.e.* damage decreases); because the material respectively loses and recovers the memory of reversible deformations (Dansereau et al., 2016). On the right-hand-side of 4, the term $\tilde{P}$, which is specific to the BBM rheology, and happens to differentiate BBM from MEB, prevents

https://doi.org/10.5194/gmd-2023-231
Preprint. Discussion started: 10 January 2024

Geoscientific Model Development
Discussions

the excessive convergence of ice when damaged:

$$\tilde{P} = \begin{cases} 0 & \text{if } \sigma_I > 0 \\ -1 & \text{if } -P_{max} < \sigma_I < 0 \\ \frac{P_{max}}{\sigma_I} & \text{if } \sigma_I < -P_{max} \end{cases}, \tag{8}$$

where $\sigma_I$ is the (isotropic) normal stress while $P_{max}$ is the ridging threshold defined as

$$P_{max} = P_0 \left(\frac{h}{h_0}\right)^{3/2} e^{-C(1-A)}. \tag{9}$$

Ólason et al. (2022) follow Dansereau et al. (2016) in using a two-step approach to solve equation 4 together with equation 1. First, an initial estimate of $\boldsymbol{\underline{\sigma}}$, noted $\boldsymbol{\underline{\sigma}}^{(\mathrm{i})}$, is calculated assuming no change in damage:

$$\partial_t \boldsymbol{\underline{\sigma}}^{(\mathrm{i})} = E\, \boldsymbol{K} \cdot \dot{\boldsymbol{\underline{\varepsilon}}} - \boldsymbol{\underline{\sigma}} \frac{1}{\lambda}\left(1 + \tilde{P}\right). \tag{10}$$

Then, as the second step, the following test and adjustment are performed on the state of stress : if $\boldsymbol{\underline{\sigma}}^{(\mathrm{i})}$ is locally overcritical, *i.e.* located outside of the *Mohr-Coulomb* damage criterion (Fig. 1), an increment in ice damage, $d_{crit}$, is applied such that

$$\boldsymbol{\underline{\sigma}} = d_{crit}\, \boldsymbol{\underline{\sigma}}^{(\mathrm{i})}, \tag{11}$$

where $\boldsymbol{\underline{\sigma}}^{(\mathrm{i})}$ is the local value of the overcritical stress, and $\boldsymbol{\underline{\sigma}}$ is the corresponding post-failure (*i.e.* post-damage) stress. As discussed in Dansereau et al. (2016), this increment in damage is calculated to allow overcritical stresses to decrease directly back to their corresponding sub-critical value, prescribed by the damage criterion, assuming viscous relaxation to be negligible during the (comparatively very fast) damage process. The associated temporal evolution of the damage and adjustment of the stress state is given by

$$\partial_t d = \frac{1 - d_{crit}}{t_d}(1 - d), \tag{12}$$

$$\partial_t \boldsymbol{\underline{\sigma}} = -\frac{1 - d_{crit}}{t_d} \boldsymbol{\underline{\sigma}}^{(\mathrm{i})}, \tag{13}$$

where $t_d$ is a characteristic time scale for damage propagation. In the case of the BBM framework, Ólason et al. (2022) and the damage criterion shown in Fig. 1 and $d_{crit}$ expresses as follows:

$$d_{crit} = \begin{cases} \dfrac{c}{\sigma_{II}^{(\mathrm{i})} + \mu \sigma_I^{(\mathrm{i})}} & \text{if } \sigma_I^{(\mathrm{i})} >= -N \\ \dfrac{-N}{\sigma_I^{(\mathrm{i})}} & \text{otherwise} \end{cases}. \tag{14}$$

where $c$ is the cohesion, and $\mu$ is the friction coefficient. The threshold $N$ is used to prevent any numerical instability at very high normal stresses and is set large enough not to impact the solution noticeably.

Finally, a slow restoring process is applied to account for the healing the ice which is associated with refreezing within open leads and which is therefore based on a rate of decrease of the damage that depends on the temperature of the ice. This process

https://doi.org/10.5194/gmd-2023-231
Preprint. Discussion started: 10 January 2024



takes the form of an extra term in equation (12), which is decoupled from the damage term thanks to the large separation of time scales between the healing and damaging processes:

$$\partial_t d = -\frac{\Delta T_h}{k_{th}} \tag{15}$$

where $\Delta T_h$ is the temperature difference between basal and surface ice and $k_{th}$ is a healing constant.

### 2.2 Numerical implementation: brittle versus viscous-plastic rheologies

To understand the extent to which the numerical implementation of a brittle rheology differs from that of a viscous-plastic one such as VP, let us first review the main differences between these rheologies and their respective classical numerical implementation.

First, the elasto-visco-brittle family of rheologies (MEB, BBM, Dansereau et al., 2016; Ólason et al., 2022) considers unfragmented sea-ice as an elastic and damageable solid. Fragmented sea-ice is a viscoelastic material in which irreversible deformations dissipate the stresses. As opposed to the VP frameworks, elasticity is therefore a physical and non-negligible component of the model, which is modulated by the level of damage, $d$, which keeps the memory of the state of fragmentation of the sea-ice cover. In non-regularized frameworks such as MEB and BBM, the combination of elasticity and damage, even if treated in an anisotropic manner, naturally simulates a strong anisotropy and localization of the deformation, down to the nominal spatial and temporal scale (*i.e.* the grid resolution and time-step of the model, respectively, Dansereau et al., 2016; Weiss and Dansereau, 2017; Rampal et al., 2019; Ólason et al., 2022). Therefore, all the mechanically-related fields, such as damage, concentration, thickness and velocity, tend to exhibit very sharp gradients, or "near-discontinuities". This is one of the reasons why, when using a staggered grid, the spatial averaging method used to relocate a field from a given type of grid point to another, becomes problematic (see section 2.3).

Second, in the BBM (as in the MEB) framework, a two-fold approach is used to linearize the system of equations and solve the coupled constitutive and damage evolution equations: (i) an initial estimate, in which stress components are updated based on the constitutive law (Eq. 10), (ii) a damage step in which the *Mohr-Coulomb* test is performed, resulting in a potential adjustment of local overcritical stresses and associated increase in local damage (Fig. 1, Eq. 12 & 13). In viscous-plastic rheologies, which do not incorporate damage, no such two-fold approach is necessary to solve the system of dynamical equations.

A third and major difference between the two types of rheology is the numerical scheme. In the VP family of rheologies, the dynamics are solved by means of an iterative approach that has to converge towards the exact solution. In BBM, however, the dynamics are solved explicitly using a time-step sufficiently small to account for the propagation of damage in the ice in a physically realistic manner. Typically, this implies using a time-step a few hundred times smaller (hereafter referred to as *small* time-step) than that used for the thermodynamics and the advection (hereafter referred to as the *big* time-step). This can be implemented by means of a *time-splitting* approach as in Ólason et al. (2022).

The fourth and last major difference between the two types of model is that in brittle models, the sea-ice internal stress tensor $\boldsymbol{\sigma}$ is a prognostic variable, while in VP, it is a diagnostic variable. This implies that the implementation of BBM in an *Eulerian*

https://doi.org/10.5194/gmd-2023-231
Preprint. Discussion started: 10 January 2024



framework, as opposed to that of a VP rheology, requires $\boldsymbol{\sigma}$ to be advected, along with other – typically scalar – tracers (see section 2.4).

### 2.3 Numerical implementation of the BBM rheology

SI3 is built upon the utilization of the finite-difference method (hereafter FD) on a staggered *Arakawa* C-grid (Arakawa and Lamb, 1977). As shown in Fig. 2.a, on the C-grid, tracers are defined at the point located at the center of each cell, hereafter referred to as the T-point. The $x$ and $y$ components of vectors are not defined at the same point, but at the center of the right-hand and upper edges of each cell, respectively (hereafter U-point and V-point). The point located at the upper-right corner of each cell, known as the vorticity point, is referred to as the F-point. In the literature, this vorticity point is sometimes located at the bottom-left corner of the cell, and is sometimes referred to as the Z-point (Losch et al., 2010; Plante et al., 2020). The U- and V-points may also be located at the left-hand and lower edges of the cell, in which case the F-point is located at the bottom-left corner of the cell (*e.g.* Losch et al., 2010).

In SI3, the use of the C-grid is justified based on numerical and practical grounds. It ensures the exact collocation of ocean and sea-ice horizontal velocity components, thereby simplifying the coupling with the ocean component of NEMO and preventing interpolation-related errors as well as extra computational load. Yet, when it comes to implementing sea-ice dynamics, using the C-grid is not the most appropriate choice because the discretized FD expressions of the elements of the strain-rate tensor $\dot{\boldsymbol{\varepsilon}}$ (Eq. 3) are staggered in space. More specifically, the trace elements, $\dot{\varepsilon}_{11}$ and $\dot{\varepsilon}_{22}$ are naturally defined at the T-point, whereas the shearing rate $\dot{\varepsilon}_{12}$ is naturally defined at the F-point.

The spatial staggering between the point definition of the normal (diagonal) and shear (off-diagonal) elements of these tensors becomes an issue whenever the parameterization of the constitutive law requires $\dot{\varepsilon}_{12}$ or $\sigma_{12}$ to be known at a T-point. This is the case, for instance, for the expression of $\Delta$ in VP models, or that of the second stress invariant $\sigma_{II}$ in BBM, as they require a value for $\dot{\varepsilon}_{12}$ and $\sigma_{12}$, respectively, at T-points. Moreover, in BBM, each component of the stress tensor is an indirect function of the ice damage, a consequence of the dependence of $E$ and $\lambda$ on $d$ (Eq. 6, 7) in the initial estimate $\underline{\boldsymbol{\sigma}}^{(\mathrm{i})}$ (Eq. 6). This implies that a value of $d$ is required not only at the T-point, but also at the F-point.

In the aEVP implementation of SI3 (Kimmritz et al., 2016), the fact that the components of the strain-rate tensor are staggered is overcome by interpolating the square of the shear rate $\dot{\varepsilon}_{12}$ from F- to T-points (as the average of the 4 surrounding F-points). Later on, the term $P/\Delta$ is also interpolated from T- to F-points in order to estimate $\sigma_{12}$. This type of spatial averaging to interpolate a field from F- to T-points, and *vice versa*, is widely used when discretizing on the C-grid. It leads to a smoothing of the relocated field, which also relates to an extra source of numerical diffusion that may or may not be acceptable depending on the problem at hand. However, in addition to being conceptually debatable in the context of a brittle model, which is expected to simulate very sharp spatial gradients, this interpolation approach, based on a four-point average, also proves to be numerically challenging. Indeed, as reported by Plante et al. (2020), and as experienced by the authors during the development of the present BBM implementation, the use of this type of interpolation across grid-points leads to spurious numerical features, such as chessboard instabilities, and an unrealistic solution.

https://doi.org/10.5194/gmd-2023-231
Preprint. Discussion started: 10 January 2024



Another limitation inherent to the discretization on the C-grid, specific to brittle rheologies, is the impossibility to advect $\sigma_{12}$ in a way consistent with that done for $\sigma_{11}$ and $\sigma_{22}$. That is because the advection of a scalar defined at the F-point, using the same scheme as that used for the advection of scalars at T-points, requires the existence of a $u$ and a $v$ at V- and U-points, respectively.

#### 2.3.1 The E-grid approach

To avoid the problems related to the staggering of the C-grid, namely the interpolation of the stress components and the damage between the center and the corner points of the grid cell, and allow the consistent advection of all the components of the stress tensor, an additional sea-ice velocity vector, noted $(\hat{u},\hat{v})$, is introduced. The x-component of this additional velocity, $\hat{u}$, is defined at V-points, while its y-component, $\hat{v}$, is defined at U-points (Fig. 2.b). Similarly, the damage tracer is also duplicated, with an additional occurrence at the upper-right corners of the grid cell, *i.e.* at F-points. This grid staggering arrangement corresponds to that of the *Arakawa* E-grid (Arakawa and Lamb, 1977; Janjić, 1984; Konor and Randall, 2018), in which tracers are defined at both the center and the four corners of the grid cell, while the two components of the velocity vector are defined at the center of the four edges of the grid cell (Fig. 2.b).

As suggested by Fig. 3.b, the E-grid can be seen as a superposition of two C-grids, in which the cell center of the additional C-grid coincides with the upper right corner of the original C-grid. For convenience, we will refer to these two grids as F-centric (additional) and T-centric (original), respectively.

In order to minimize the number of modifications and rewriting in the SI3 code, the idea was to restrict the use of this *E-augmented* C-grid to the rheology/dynamics module only. The rest of the code, which includes the thermodynamics, remains unmodified and relies entirely on the standard C-grid. As such, only rheology-specific tracers are defined in the E-grid fashion, *i.e.* at both T- and F-points. In our case, this applies only to the ice damage $d$ and components of the internal stress tensor (even though components of a tensor cannot be considered exactly as tracers when it comes to the advection, see section 2.4). However, global tracers, such as ice concentration and thickness, which are updated within the thermodynamics module, remain defined at the T-point only. Consequently, these tracers are interpolated at the F-point within the rheology module whenever needed.

To summarize, in the proposed rheology-specific *E-augmented* C-grid approach, as shown in figure 3, the conventional C-grid model variables are augmented with: (i) the u-velocity component at V-points and v-velocity component at U-points, (ii) the ice damage, $\sigma_{11}$ and $\sigma_{22}$ at F-points, and (iii) $\sigma_{12}$ at T-points. This approach implies that most of the equations related to the dynamics, including constitutive and momentum equations, as well as the advection, have to be solved on both the T- and F-centric grids. As detailed in Appendix B, the exact same discretization and numerical schemes can be used on both grids, with only the indices of the velocity components on the F-centric grid requiring particular attention: $\hat{u}_{i+1,j}$ and $\hat{v}_{i,j+1}$ have to be used as the counterparts of $u_{i,j}$ and $v_{i,j}$ on the T-centric grid (Fig.3.b). This is true for the computation of the strain-rate tensors (B2.1), constitutive equation (B2.2), momentum equation (B3), divergence of the stress tensor (B3.1), advection, etc.

At this stage it is important to note that the doubling of the number of computational points implied by the transition to the E-grid, in no way relates to an increase of the spatial resolution of the original C-grid. Because the FD discretization of spatial

https://doi.org/10.5194/gmd-2023-231
Preprint. Discussion started: 10 January 2024

Geoscientific Model Development
Discussions

derivatives on the E-grid (see Appendix B) still relies on the same local spatial increment, *i.e.* $\Delta x$, as that of the original C-grid, regardless of the sub-grid considered (T- or F-centric).

#### 2.3.2 The separation of solutions and how it is restrained

Thanks to the *E-augmented C-grid* approach, all rheology-specific prognostic variables are defined at the points where their value is required, and no interpolation is needed to solve the equations. It does, however, result in an apparent over-determination, which allows the T- and F-centric solutions to evolve somewhat independently from one another. This separation of solutions rapidly degenerates into unrealistically noisy solutions as the spatial consistency of the fields between the two grids deteriorates.

This problem of grid separation has been known since the early adoption of the E-grid by the community (Arakawa, 1972; Mesinger, 1973; Janjić, 1974; Janjić and Mesinger, 1983; Mesinger and Popovic, 2010), in particular, in the context of the shallow-water equations. Various treatments and methods have been proposed, from filtering approaches to more advanced ones such as the introduction of auxiliary velocity points, midway between the neighboring tracer points (Mesinger, 1973; Janjić, 1974). Recently, Konor and Randall (2018) have mentioned the need to introduce a "horizontal mixing process" to avoid the "separation of solutions" when using the E-grid.

The cause of the separation of the two solutions resides in the weak coupling between the two grids, as they only exchange very little information. Specifically, in our case, the only exchange of information between the T- and F-centric grids occurs via the ice velocity vector: in the *Coriolis* term of the momentum equation (Eq. 1), and in the upper-convected time derivative (*i.e.* advection) of the stress tensors (see section 2.4). Due to the relatively small contribution of these two terms, this exchange of information cannot prevent the decoupling of the solutions between the two grids. Hence, a numerical treatment is required to constrain the T- and F-centric solutions to remain spatially consistent with one another.

During the early phase of our development, we considered, implemented, and tested a variety of such treatments. So far, only one has proven able to prevent the grid separation issue without leading to noisy and/or unrealistic solutions. This treatment, which operates on the T- and F-centric stress tensors at the *small* time-step level, will hereafter be referred to as the *cross-nudging*. It consists in nudging each component of the T-centric stress tensor $\boldsymbol{\sigma}$ towards its F-centric counterpart (in tensor $\hat{\boldsymbol{\sigma}}$) interpolated at the relevant point under even time-step integrations, and conversely under odd time-step integrations. This nudging is achieved by means of the two following equations:

$$\begin{aligned}
\begin{pmatrix}\sigma_{11}\\ \sigma_{22}\\ \sigma_{12}\end{pmatrix} &= \gamma_C\,\frac{\Delta t}{\Delta T}\begin{pmatrix}\sigma_{11}-\texttt{interpF@T}(\hat{\sigma}_{11})\\ \sigma_{22}-\texttt{interpF@T}(\hat{\sigma}_{22})\\ \sigma_{12}-\texttt{interpT@F}(\hat{\sigma}_{12})\end{pmatrix} &&\text{(even time-step )}\\
\begin{pmatrix}\hat{\sigma}_{11}\\ \hat{\sigma}_{22}\\ \hat{\sigma}_{12}\end{pmatrix} &= \gamma_C\,\frac{\Delta t}{\Delta T}\begin{pmatrix}\hat{\sigma}_{11}-\texttt{interpT@F}(\sigma_{11})\\ \hat{\sigma}_{22}-\texttt{interpT@F}(\sigma_{22})\\ \hat{\sigma}_{12}-\texttt{interpF@T}(\sigma_{12})\end{pmatrix} &&\text{(odd time-step )}
\end{aligned}\tag{16}$$

in which $\gamma_C$ is the cross-nudging coefficient. As the interpolation methods, denoted by `interpF@T` and `interpT@F`, the usual average of the value at the four nearest surrounding cell corners (F- and T- points, respectively) is used (see Eq. A1

https://doi.org/10.5194/gmd-2023-231
Preprint. Discussion started: 10 January 2024



in Appendix A4), which inevitably leads to a smoothing of the solution in space. As such, $\gamma_C$ , is chosen to achieve the best compromise between smoothing and coupling of the T- and F-centric solutions. Here too, sensitivity tests have been performed, and we conclude that the right compromise is achieved when $\gamma_C$ typically lies between 1 and 3, with 2 being the value used in our experiments. As illustrated in figure 5, with a value below 1, the solutions becomes increasingly noisy as $\gamma_C$ approaches zero. In particular, the damage field tends to exhibit strongly unrealistic straight-line features of high damage that are horizontally and vertically aligned with the grid cells. Values of $\gamma_C$ beyond 3 lead to excessive smoothing of the solutions, without the benefit of better coupling between the the T- and F-centric solutions; because the spatial consistency between these solutions typically starts to plateau from about $\gamma_C$ =2.

### 2.4 Horizontal advection

In neXtSIM, the *Lagrangian* finite-element model used by Ólason et al. (2022), the advection occurs implicitly at each model time-step (also corresponding to the thermodynamics time-step) through the ice-velocity-driven displacement of the mesh elements. As such, the rate of change of a prognostic scalar $\phi$ is $\dot{\phi} \equiv \partial_t \phi$. In the present *Eulerian* context, however, the term relative to the horizontal advection has to be considered so that the rate of change of $\phi$ is now $\partial_t \phi + U\,\partial_x \phi + V\,\partial_y \phi$. In our implementation, as pointed out by Ólason et al. (2022), this advection term is computed and added to the trend of the prognostic scalar considered every *big* time-step. Thus, the sea-ice velocity vector $U,V$ we consider for the advection, at the *big* time-step level, is the mean of the $N_s$ successive velocity vectors $(u,v)$ calculated under one time-splitting instance. $U,V$ can also be seen as the sum of the $N_s$ successive displacement vectors, hence the total displacement vector during one *big* time-step, divided by the big time-step.

We use the *second-order-moments-conserving* advection scheme of Prather (1986) available in SI3 to advect the damage and the components of the stress tensors (considered as scalar for now, see section 2.4.1). Technically, the damage and stress tensor components defined at the T-point ($d$, $\sigma_{11}$, $\sigma_{22}$ and $\hat{\sigma}_{12}$) are advected using $U$ and $V$ defined at U- and V-points, respectively. Their F-point counterparts ($\hat{d}^F$, $\hat{\sigma}_{11}$, $\hat{\sigma}_{22}$ and $\sigma_{12}$) are advected using $\hat{U}$ and $\hat{V}$ defined at V- and U-points, respectively. In practice, the exact same implementation of the advection scheme can be used to perform the advection at T- and F-points; the only difference being that for the advection of F-point scalars, the spatial indexing of the velocity components is staggered by 1 cell. Namely, $\hat{U}_{i+1,j}$ and $\hat{V}_{i,j+1}$ have to be used in place of $U_{i,j}$ and $V_{i,j}$ (Fig. 3.b).

As it is commonly done in sea-ice models, and justified by a scale analysis of the momentum equation, the term for the advection of momentum is neglected.

#### 2.4.1 Advection of the sea-ice internal stress tensor

With respect to that of a scalar, the rate of change of a tensor in the *Eulerian* framework, known as the *upper-convected* time derivative, includes additional terms to account for the deformation of the medium, here in the form of a symmetric tensor $\boldsymbol{L}$:

$$\overset{\triangledown}{\boldsymbol{\sigma}} \equiv \partial_t \boldsymbol{\sigma} + \left(\vec{U}.\vec{\nabla}\right)\boldsymbol{\sigma} - \boldsymbol{L} \tag{17}$$

https://doi.org/10.5194/gmd-2023-231
Preprint. Discussion started: 10 January 2024

Geoscientific Model Development
Discussions

with

$$\boldsymbol{L} = \left(\vec{\nabla}\vec{U}\right) \cdot \boldsymbol{\sigma} + \boldsymbol{\sigma} \cdot \left(\vec{\nabla}\vec{U}\right)^T, \tag{18}$$

which, in component form, reads

$$\begin{aligned} L_{11} &= 2\left[\dot{\varepsilon}_{11}\ \sigma_{11} + \partial_y U\ \sigma_{12}\right] \\ L_{22} &= 2\left[\dot{\varepsilon}_{22}\ \sigma_{22} + \partial_x V\ \sigma_{12}\right] \\ L_{12} &= \left(\dot{\varepsilon}_{11} + \dot{\varepsilon}_{22}\right)\ \sigma_{12} + \partial_x V\ \sigma_{11} + \partial_y U\ \sigma_{22} \end{aligned} \tag{19}$$

In our implementation, as mentioned earlier, each component of the stress tensors is first advected like a scalar, providing the first contribution of the advection term $(\vec{U}.\vec{\nabla})\boldsymbol{\sigma}$ in Eq. 17. Then, the tensor-specific contribution $-\boldsymbol{L}$ is added.

# 3 Model Evaluation

## 3.1 Model setup

We use the version 4.2.1 of the NEMO modeling system (Madec et al., 2022) as the basis for the development of the BBM rheology code extension, and for carrying out the coupled ocean/sea-ice hindcast simulations to be assessed. These coupled simulations involve the 3D-ocean and sea-ice components of NEMO: namely OCE and SI3. SI3 is the default sea-ice component of NEMO since version 4 (Vancoppenolle et al., 2023). It largely inherits from LIM3 Rousset et al. (2015), to which it succeeds, with some significant inclusions from CICE (Hunke et al., 2017) and GELATO (Mélia, 2002).

Our simulations are performed on the so-called NANUK4 regional configuration, which is an Arctic extraction of the standard global 1/4°resolution NEMO gridded horizontal domain known as ORCA025 (Barnier et al., 2006). As such, and as shown in Figure 4, the actual grid resolution of NANUK4 typically spans 10 up to 14 kilometers in the central Arctic region. NANUK4 features two open lateral boundaries; the southernmost boundary is located at about 39°N in the Atlantic ocean, while the second boundary is located south of the Bering Strait, at about 62°N in the Pacific ocean. The vertical $z$-coordinate grid used for the ocean features 31 levels with a $\Delta z$ of 10 m at the surface up to about 500 m at the deepest level, at a depth of 5250 m.

Hindcast simulations are achieved through the use of interannual surface (atmospheric) and lateral (3D ocean) forcings. For the atmospheric forcing, both the ocean and the sea-ice components receive, as surface boundary conditions, fluxes of momentum, heat and freshwater at the air-sea and air-ice interface, respectively. These fluxes are computed every hour by means of bulk formulae using the hourly near-surface atmospheric state from the ERA5 reanalysis of the ECMWF (Hersbach et al., 2020) and the prognostic surface temperature of the relevant component (SST or ice surface temperature).

For the lateral boundary conditions of OCE, the 3D ocean is relaxed towards the monthly-averaged 3D horizontal velocities, temperature, salinity and SSH (2D) of the GLORYS2 [1] ocean reanalysis version 4 (Ferry et al., 2012).

[1] https://data.marine.copernicus.eu/product/GLOBAL_REANALYSIS_PHY_001_031/description

https://doi.org/10.5194/gmd-2023-231
Preprint. Discussion started: 10 January 2024


Both OCE and SI3 use a time-step of $\Delta T$ =720 s, the *big* time-step. The coupling between these two components is also done at each *big* time-step.

### 3.2 Experimental design

We carried out a twin coupled ocean/sea-ice hindcast, with one experiment using the *aEVP* rheology of Kimmritz et al. (2016) (corresponding to the default option in SI3), and the second experiment using our current implementation of the BBM rheology (hereafter referred to as SI3-aEVP and SI3-BBM, respectively). These two experiments were spun-up following a two-segment spin-up strategy. In the first segment, each experiment has been run for 10 months, spanning January 1$^{st}$ to October 31$^{st}$ 1996. As initial conditions for January 1$^{st}$ 1996, OCE was initialized at rest (no current) with the 3D temperature/salinity state taken from the GLORYS2v4 reanalysis, while SI3 was initialized with a constant ice thickness of 1.5 m and a sea-ice concentration of 100 % over regions with a SST below or equal to -2°C.

For the second spin-up segment, spanning November 1$^{st}$ to December 15$^{th}$ 1996, OCE was *restarted* using the ocean restart spawned October 31$^{st}$ 1996. SI3, instead, underwent a fresh initialization, in which the sea-ice concentration, thickness, and damage (only for SI3-BBM) were extracted from a coupled OCE-neXtSIM simulation performed at the same spatial resolution and using the same BBM rheology to solve sea-ice dynamics (Boutin et al., 2023). This *November-to-mid-December* 1996 simulation segment is thereby regarded as the second and final spin-up segment, with a duration sufficiently long for the coupled system to recover from the *ad-hoc* reinitialization.

Finally, the actual production segment, spanning December 15$^{th}$ 1996 to April 20$^{th}$ 1997, was initialized using the restarts obtained at the end of the second spin-up segment.

For these experiments, the tuning of SI3 is kept as close as possible to the default *namelist* of version 4.2.1. As such, thermodynamics features 5 ice-categories. Yet, a few modifications are done (summarized in table 1). The ice-atmosphere drag coefficient, $C_{Da}$, has been adjusted so that the mean deformation rate at the 10 km scale simulated in each experiment is in agreement with that derived from the satellite observations against which we evaluate the model in section 3.3. The value of the parameters specific to the BBM rheology that we use in SI3-BBM are given in Table A1 in appendix C. As mentioned in section 2.2 the BBM rheology relies on a time-splitting approach for solving the momentum equation. We use a *small* time-step of 4 s in SI3-BBM, which relates to a time-splitting by a factor $N_s$ =180. For SI3-aEVP, the number of iterations is increased from the default value of 100 to 180 in order to slightly improve the numerical convergence of the solution, as well as to allow a fairer comparison between the two experiments in terms of computational cost (discussed in section 4).

### 3.3 Construction of observation-based and simulated *Lagrangian* sea-ice deformations

Our assessment of the numerical implementation of the BBM rheology into SI3 relies on a multiscale statistical analysis. This analysis, which focuses on winter 1996-1997, compares the sea-ice deformation rates constructed from the RADARSAT Geophysical Processor System Lagrangian trajectories dataset of Kwok et al. (1998) (RGPS hereafter) to their simulated counterparts.

Geoscientific Model Development
Discussions

The preprocessing and computing approach we use to construct sea-ice deformations out of the raw RGPS *Lagrangian* trajectories is detailed in Appendix C2. It is very similar to that used by Ólason et al. (2022), the main difference being that it relies on the tracking of quadrangles rather than triangles.

The simulated counterparts of the RGPS trajectories are constructed using Eulerian sea-ice velocities simulated by SI3 in the two experiments discussed in section 3.2. To do so, we use a *Lagrangian* tracking software that we developed for this purpose (see the *Code and data availability* section. As further detailed in Appendix C2.4, the tracking software seeds the same points as those involved in the definition of the quadrangles selected for computing the RGPS deformation, respecting their initial position in space and time. These points are then tracked for about three days, using the hourly-averaged *Eulerian* sea-ice velocities of SI3; the exact tracking duration used being that of the time interval between the two consecutive positions of the corresponding RGPS point.

### 3.4 Results

#### 3.4.1 Probability density function of sea-ice deformation rates

As illustrated by the maps of the 3-day total deformation rates shown in figure 6, RGPS clearly exhibits narrow and long features (commonly called *Linear Kinematic Features* or *LKF* in the literature) along which the deformation is concentrated. Visually, LKF simulated by SI3-BBM are quite realistic, both in terms of length and orientation, and the magnitude of the deformation rates along these LKF is similar to that of RGPS. SI3-aEVP, however, exhibits very smooth fields of deformation with no such localized features; this is consistent with the findings of recent studies that evaluate VP-driven sea-ice simulations run with a horizontal grid size larger than a few kilometers (*e.g.* Ólason et al., 2022; Bouchat et al., 2022).

The probability density functions (hereafter PDFs) of the total deformation rates depicted in figure 7.d show that SI3-BBM exhibits a power-law tail similar to that of RGPS over the values corresponding to the last two percentiles of the RGPS distribution, although with different exponents (-2.9 and -3.3, respectively). Such an exponent over that same range of values cannot be estimated for the SI3-aEVP distribution because of the absence of a power-law tail. A look at the other invariants of the deformation (*i.e.* shear, divergence and convergence rates) in figure 7.a,b,c) shows that Si3-BBM is consistently more likely to simulate large deformation events than Si3-aEVP, which suggests the advantage of BBM over aEVP for capturing the heterogeneous character of sea-ice deformation in our setup.

Indeed, the extreme values of deformation rates are, if not absent, largely underestimated in Si3-aEVP, as highlighted by the departure between the observed and simulated PDFs shown as color bars below each panel of figure 7. We note that both simulations are unable to reproduce the observed convergence over the full range of values present in the RGPS data (Fig. 7.c). Nevertheless SI3-BBM clearly demonstrates higher skills than Si3-aEVP in capturing the extreme values.

#### 3.4.2 Time-series of sea-ice deformation rates

Following Ólason et al. (2022), we analyze the 90$^{th}$ percentile of total deformation (P90), as this is a metric sensitive to the high values that shape the long tail of the PDFs of deformation. P90 is the value of deformation below which 90% of deformation

https://doi.org/10.5194/gmd-2023-231
Preprint. Discussion started: 10 January 2024



values in the frequency distribution fall. P90 is computed from each snapshot of deformation from mid-December 1996 to late April 1997 to evaluate the temporal evolution of the deformation. Values of P90 from RGPS, SI3-BBM and SI3-aEVP are plotted and inter-compared using the bias ($b$), root mean square error (RMSE, $e$), and the *Pearson* correlation coefficient ($\rho$). In addition to the 90$^{\text{th}}$ percentile, we also consider the 95$^{\text{th}}$ and 98$^{\text{th}}$ percentiles.

As illustrated in figure 8, here too SI3-BBM demonstrates better skills than SI3-aEVP by being in better agreement with the observations, both in terms of magnitude and correlation (see table 2). The biases and RMSEs are consistently lower for SI3-BBM than for SI3-aEVP and the correlation coefficient is higher. Also, the higher the percentile value, the better the agreement of SI3-BBM with the observations, which indicates, again, that BBM is better than aEVP at simulating very large deformation events.

#### 3.4.3 Multifractal scaling analysis

The presence of heavy tails in the distributions shown in figure 7 implies that one needs to consider higher moments than the mean to fully describe the statistics of the sea-ice deformation process (Sornette, 2006). Following Marsan et al. (2004), the calculation of moments should be limited to those of order $q > 0$, because zero values exist in the deformation field. And they should not exceed the order $q = 3$ since a transition is observed between typically $q_c = 2.5$ and $q_c = 3$ (Schertzer and Lovejoy, 1987). The reason for this is that the tails of the distributions for RGPS and SI3-BBM follow a power-law decay with an exponent of about -3, hence their moments of order $q > q_c$ diverge.

We performed a multifractal spatial scaling analysis of the RGPS total deformation rates and their simulated counterparts, considering the moments $q = 1$, 2 and 3 of the distributions. As shown in figure 9, both the observed and simulated statistics (mean, variance, and skewness) are following power-laws. Interestingly, the observed mean sea-ice deformation rate $\langle \dot{\varepsilon} \rangle$ is particularly well reproduced in SI3-BBM across the full range of spatial scales considered for this analysis, and can be approximated by a power-law scaling $\langle \dot{\varepsilon} \rangle \sim L^{-\beta}$, where $L$ is the spatial scale and $\beta$ an exponent of about 0.15. As previously mentioned in the section 3.2, we note that both SI3-BBM and SI3-aEVP have been tuned to reproduce the same mean deformation rate as the observations at the nominal scale of 10 km, which led to the use of different values for the atmospheric drag coefficients ($C_{Da}$ =1.65 10$^{-3}$ in SI3-BBM, and $C_{Da}$ =1.15 10$^{-3}$ in SI3-aEVP). However, the higher moments, which characterize the largest and most extreme values of the distributions, remain underestimated in both SI3-BBM and SI3-aEVP compared to the observations.

Indeed, the exponents of the power-law that fits the SI3-BBM data ($\beta$ =-0.52 and -1.18, for $q = 2$ and 3, respectively) are lower than those of the observations ($\beta$ =-0.70 and -1.51). These same exponents however are even smaller for SI3-aEVP ($\beta$ =-0.13 and -0.35). This indicates that SI3-BBM is better than SI3-aEVP in capturing the strength of the spatial scaling of sea-ice deformation revealed by the observations, which can also be seen as the degree of localization of the sea-ice deformation.

Finally, we note that the spatial scaling of the sea-ice deformation simulated in SI3-aEVP does not hold over the full range of scales we consider here, but seems to break for scales larger than about 300 km.

The simulated and observed structure functions (*i.e.* the dependence of the scaling exponents of the power-law to the order of the moment) $\beta(q)$ are shown in Figure 10. The spatial scaling obtained from both the observations and our simulations are

https://doi.org/10.5194/gmd-2023-231
Preprint. Discussion started: 10 January 2024



multi-fractal, because their structure functions is well approximated (in the sense of the least square method) by a quadratic function of the type $\beta(q) = aq^2 + bq$. One should note that in the universal multi-fractal formalism, the structure functions are not required to be quadratic and can have a varying degree of non-linearity (Lovejoy and Schertzer, 2007). A quadratic structure function, as obtained here, simply means that the process of sea-ice deformation can be approximated by a log-normal multiplicative cascade model with a maximum degree of multi-fractality. However, only the structure function of SI3-BBM shows a curvature $a$ that has a magnitude sufficiently large and comparable to that of RGPS, *i.e.* 0.13 versus 0.17. These values of curvature are in line with those obtained from *Lagrangian* simulations performed with neXtSIM, and reported in previous studies: 0.14 in Rampal et al. (2016) and 0.11 in Rampal et al. (2019).

## 4 Discussion

### 4.1 On the numerical implementation

A critical requirement for the consistent implementation of the brittle rheology when using the finite-difference discretization method combined with the *Arakawa* C-grid, is the need to refrain from using spatial interpolation of prognostic fields between points of the grid that are staggered in space. The switch to the E-grid satisfies this requirement but introduces a new issue inherent to this type of grid: the spatial separation of the two solutions. We have overcome this issue by introducing a nudging on the two stress tensors. This spatial cross-nudging bears a noteworthy analogy with the *Asselin* filter (Asselin, 1972) used when discretizing time derivatives of a prognostic variable by means of the *Leap Frog* scheme (three time-levels, centered, and second-order), in particular in the context of shallow-water equations. The goal of this *Asselin* filter is to subtly average the solutions of neighboring time levels to prevent the separation of trajectories between the even and odd time-step levels (Marsaleix et al., 2012). As such, the cross-nudging can be seen as a sort of spatial and two-dimensional analogue to the *Asselin* filter. Despite the crudeness of this approach, which tends to be problematic due to the unavoidable loss of conservation properties, the *Asselin* filter is still largely used in modern CMIP-class OGCMs like NEMO. Indeed, the ocean component of NEMO used in the simulations presented in this study still relies on it. Therefore, despite the lack of physical and numerical consistency of our cross-nudging approach, we think that it serves a useful purpose by allowing to demonstrate that the implementation of a brittle rheology is feasible onto an *E-augmented* C-grid. Nevertheless, we plan to further investigate the possibility to implement approaches that are more physically and numerically consistent. For instance, an option is to apply the cross-nudging on the two invariants of the stress tensor (*i.e.* $\sigma_I$ and $\sigma_{II}$) and the rate of internal work of the ice. This would introduce 3 equations for 3 invariant quantities, from which the 3 components of the stress tensor could be deduced afterward. Another option, is to explore the possibility of deriving a numerical formulation inspired from that of Mesinger (1973); Janjić (1974), in which auxiliary velocity (or stress) points are introduced midway between the neighboring tracer (or velocity) points.

Another critical requirement, this time stemming from the use of the *Eulerian* and finite-difference framework, has to do with the ability of the advection scheme to advect fields with as little numerical diffusion or dispersion as possible. This is particularly critical when using a brittle rheology like BBM, as most fields exhibit sharp gradients, often associated with linear kinematic features. We chose to use the scheme of Prather (1986), the *dispersive scheme* option of SI3, to favor the

https://doi.org/10.5194/gmd-2023-231
Preprint. Discussion started: 10 January 2024



conservation of sharp gradients at the cost of potential noise and overshoots reminiscent of the *Gibbs* phenomenon. One could however consider the use of a different approach, which would optimize the advection of sharp gradients, for instance a spatial discretization based on the discontinuous *Galerkin* method. This method has proven to be efficient and accurate in treating the advection of sea-ice variables in the case of a brittle sea-ice rheology such as MEB (Dansereau et al., 2017), but has not yet been tested in the context of large scale, long-term sea-ice simulations. This is the scope of our present work and future papers.

As discussed in section 2.3.1, the use of the E-grid in the dynamics and advection modules of SI3 implies that equations specific to the momentum and the constitutive law are solved twice, on the T- and F-centric grids. Moreover, with the need to advect the stress tensor and the damage tracer, specific to brittle rheologies, 2×4 additional scalar fields need to be advected. This inevitably leads to an increase in the computational cost of SI3. We have estimated this extra cost by comparing the wall time length required to complete a 4-month simulation with each rheology, using the same 29 cores in parallel, on the same computer. Our results, that are summarized in table 3, suggest that the increase in the computational cost associated with the use of BBM in place of aEVP is about 60% when SI3 is used in a standalone mode. When SI3 is coupled to OCE, however, the cost increase is somehow dissolved by the overwhelming cost of OCE and falls below 30%. Note that this later figure is expected to substantially decrease as the number of ocean levels used in OCE is increased. Our choice to use 31 levels rather than the 75 levels traditionally used in 1/4°NEMO configurations, has been motivated by the need to have a lighter 3D ocean component to handle during the development phase.

Since SI3 is mainly intended to be run coupled to OCE, and given the significant improvements in the simulated sea-ice deformation discussed in section 3.4, we think that the extra computational cost induced by the use of the BBM rheology is justified and acceptable. Moreover, it is worth noting that despite the use of 180 iterations in the SI3-aEVP simulation (100 by default in SI3), we noticed recurring chessboard instabilities patches in simulated fields such as the sea-ice internal stresses. We have verified the link between these numerical instabilities and an insufficient number of iterations, as the instabilities vanish when a sufficiently large number of iterations is used (typically about 1000). In that regard, the computational cost of a fully-converged aEVP would largely exceed that of our current BBM implementation.

### 4.2 On the simulated sea-ice deformations

Large-scale realistic sea-ice simulations performed with a model using the BBM rheology (other than SI3) have already been assessed against observations and have shown very promising results (Ólason et al., 2022; Boutin et al., 2023), like for instance about the Arctic sea-ice thickness distribution. Yet, BBM does not seem to simulate the subgrid-scale process related to sea-ice ridging well enough. This indicates that the convergent deformation at the local – model grid – scale is not represented in a fully consistent manner. As shown on the PDF in figure 7.c, the model largely overestimates the number of converging events with magnitudes of about 1 to 5% per day, and slightly underestimates the most extreme events (we note that this is even more true with aEVP). This problem was already reported in Ólason et al. (2022), and based on various sensitivity experiments, we came to the conclusion that it cannot be solved through the tuning of model parameters. In particular, the sensitivity to the BBM-specific *ridging threshold* parameter $P_{max}$, whose only purpose is to control the basin-scale sea-ice convergence, and thus the thickness of the sea-ice cover at large scale, has been extensively investigated.

https://doi.org/10.5194/gmd-2023-231
Preprint. Discussion started: 10 January 2024

Geoscientific Model Development Discussions

In section 3.4.3, we find that the degree of multi-fractality of the deformation fields simulated by SI3-BBM is slightly lower than that obtained from the RGPS data. The fact that the sea-ice deformation fields simulated by neXtSIM in Ólason et al. (2022) are doing better in this particular matter suggests that this propensity of SI3-BBM to underestimate the degree of multi-fractality is linked to some numerical aspects of our BBM implementation, and not the BBM rheology itself. The best candidates are likely to be a combination of the additional source of numerical dispersion and diffusion, related to the advection and cross-nudging steps, respectively, as these steps are absent in neXtSIM. Moments of order two and three are expected to be more affected than the mean by an unwanted source of noise and diffusion, which might explain why SI3-BBM reproduces remarkably well the mean across all scales, and why the power-law exponents for the variance and the skewness are underestimated. In this regard, the use of the finite-element method together with the *Discontinuous Galerkin* method, might prove to be a relevant combination to simulate sea-ice deformation while remaining in the *Eulerian* and quadrilateral mesh framework.

## 5 Conclusions

The *Brittle Bingham Maxwell* rheology, known as BBM, has been successfully implemented into SI3, the CMIP-class, Eulerian finite-difference sea-ice model of the NEMO modeling system. To our knowledge, it is the first implementation of a brittle rheology, featuring a prognostics ice damage tracer, that is able to produce a realistic solution on a pan-Arctic scale when constructed upon this type of numerical framework. The use of the Arakawa C-grid, as used in SI3, has proven to be poorly fitted for brittle rheologies. This is mainly due to (i) the staggering between the trace and shearing elements of the discretized strain-rate and stress tensors, and (ii) the requirement for the stress tensor to be advected along with traditional prognostic sea-ice variables. To overcome these limitations, we propose to augment the C-grid into an E-grid in the parts of the solver dedicated to the dynamics, *i.e.* in the rheology and advection modules. This approach prevents the numerical schemes at play in the rheology and the advection to heavily rely on fields interpolated between the center and corner points of the grid meshes, which proved to be a major obstacle during the early phase of our implementation, as they consistently lead to degraded or/and unrealistic solutions. It also allows the thorough advection of prognostic fields defined at corner points of the mesh.

We carried out a statistical analysis of the sea-ice deformation rates obtained from a set of realistic pan-Arctic coupled ocean/sea-ice simulations of winter 1996-1997, performed with SI3 at a horizontal resolution of about 12-km. Based on a comparison with satellite observations, this analysis demonstrates that the use of the newly implemented BBM rheology, in place of the default viscous-plastic rheology of SI3, results in simulated sea-ice deformations that are consistently more realistic. In particular, we show that with respect to the viscous-plastic rheology, the use of BBM allows to simulate highly-localized (nearly linear) kinematic features within the sea-ice cover, along which the most substantial deformation rates are concentrated.

The observed non-*Gaussian* statistics of the sea-ice deformation process, expressed by the presence of heavy tails in the PDF of deformation rates, are also reproduced in the simulation that uses our newly-implemented BBM rheology. Finally, we also

https://doi.org/10.5194/gmd-2023-231
Preprint. Discussion started: 10 January 2024

Geoscientific Model Development Discussions
Open Access
EGU

show that the observed spatial scaling invariance property of sea-ice deformation, and in particular its multi-fractal nature, is also well –although not fully– captured by the BBM-driven simulation.

Based on our results, we conclude that the ability of a continuous sea-ice model to simulate the complex sea-ice dynamics across scales, as observed from satellites, depends primarily on the type of rheology used rather than on the type of modeling formalism chosen (*i.e. Eulerian* versus *Lagrangian*). As such, the newly-implemented BBM rheology allows SI3 to simulate sea-ice dynamics with a level of realism comparable to that of the *Lagrangian* sea-ice model neXtSIM.

*Code and data availability.*

The NEMO source code used in the experiment is based on the tagged version 4.2.1, available from the official GitLab NEMO depository: https://forge.nemo-ocean.eu/nemo/nemo.

```
» git clone -b '4.2.1' git@forge.nemo-ocean.eu:nemo/nemo.git
```

New and modified Fortran-90 source files relative to our implementation of the BBM rheology in version 4.2.1 of NEMO/SI3 will be made available, upon publication of the present paper, in a dedicated branch of the official GitLab NEMO depository.

The python software used to seed and build *Lagrangian* trajectories out of the SI3 hourly sea-ice velocities is named `sitrack` and is available in the following GitHub repository of the lead author:
https://github.com/brodeau/sitrack

The python software used to compute the RGPS and model-based sea-ice deformation rates based on quadrangles, and perform the scaling analysis, is named `mojito` and is available in the following GitHub repository of the lead author:
https://github.com/brodeau/mojito

Model data produced and analyzed in this study, namely SI3 1-hourly and 6-hourly output files for simulations SI3-BBM and SI3-aEVP, are downloadable from the following OpenDAP server:
https://ige-meom-opendap.univ-grenoble-alpes.fr/thredds/catalog/meomopendap/extract/SASIP/model-outputs/BROD2024/catalog.html

*Video supplement.* Videos that illustrate the difference of behavior between SI3-aEVP and SI3-BBM will be uploaded online and freely accessible upon publication.

https://doi.org/10.5194/gmd-2023-231
Preprint. Discussion started: 10 January 2024

Geoscientific Model Development
Discussions

## Appendix A: Nomenclature

### A1 Table of symbols used in the text

| Symbol | Definition | Units |
|---|---|---|
| $m$ | mass of snow and sea-ice per unit area | [kg m$^{-2}$] |
| $\rho_i$ | density of sea-ice | [kg m$^{-3}$] |
| $\rho_w$ | density of sea-water | [kg m$^{-3}$] |
| $\vec{u} \equiv (u,v)$ | sea-ice velocity | [m s$^{-1}$] |
| $A$ | sea-ice fraction | [-] |
| $h$ | sea-ice thickness | [m] |
| $g$ | acceleration of gravity | [m s$^{-2}$] |
| $f$ | *Coriolis* frequency | [s$^{-1}$] |
| $H$ | sea surface height | [m] |
| $\vec{\tau}$ | ice-ocean stress | [Pa] |
| $\vec{\tau}_a$ | wind (ice-atmosphere) stress | [Pa] |
| $\boldsymbol{\sigma}$ | internal stress tensor (2×2) | [Pa] |
| $\dot{\boldsymbol{\varepsilon}}$ | strain-rate tensor (2×2) | [s$^{-1}$] |
| $d$ | damage of sea-ice | [-] |
| $\Delta x$ | local resolution (size) of the grid mesh | [m] |
| $C$ | compaction parameter | [-] |
| $\alpha$ | damage parameter (Dansereau, 2016) | [-] |
| $E_0,\ E$ | elasticity of undamaged and damaged sea-ice | [Pa] |
| $\lambda_0,\ \lambda$ | viscous relaxation time of undamaged and damaged sea-ice | [s] |
| $\tilde{P}$ | BBM-specific ridging term | [-] |
| $P_{max}$ | ridging threshold | [Pa] |
| $P_0$ | scaling parameter for $P_{max}$ | [Pa] |
| $h_0$ | reference ice thickness for $P_{max}$ | [m] |
| $c$ | sea-ice cohesion | [Pa] |
| $\nu$ | Poisson's ratio | [-] |
| $\sigma_I$ | isotropic normal stress (first invariant of stress tensor) | [Pa] |
| $\sigma_{II}$ | maximum shear stress (second invariant of stress tensor) | [Pa] |
| $\mu$ | internal friction coefficient | [-] |
| $N$ | upper limit for compressive stress | [Pa] |
| $t_d$ | characteristic time scale for the propagation of damage | [s] |
| $d_{crit}$ | damage increment (Dansereau, 2016) | [-] |
| $k_{th}$ | healing constant for damage | [K s] |
| $\Delta T_h$ | temperature difference between bottom and surface of ice | [K] |

https://doi.org/10.5194/gmd-2023-231
Preprint. Discussion started: 10 January 2024

Geoscientific Model Development Discussions
Open Access

### A2 Acronyms

| | |
|---|---|
| NEMO | Nucleus for European Modeling of the Ocean |
| SI3 | Sea-Ice modeling Integrated Initiative (sea-ice component of NEMO) |
| OCE | 3D ocean component of NEMO |
| LIM | Louvain-La-Neuve sea-Ice Model |
| BBM | Brittle Bingham Maxwell (rheology) |
| MEB | Maxwell Elasto Brittle (rheology) |
| VP | Viscous-Plastic (rheology) |
| FD | Finite Difference (method) |
| PDF | Probability Density Function |
| LKF | Linear Kinematic Features |
| OGCM | Ocean General Circulation Model |
| SST | Sea Surface Temperature |
| SSH | Sea Surface Height |
| RGPS | RADARSAT Geophysical Processor System (dataset) |

### A3 Miscellaneous notations

| | |
|---|---|
| $\underset{\sim}{\boldsymbol{x}}$ | symmetric 2×2 tensor $\boldsymbol{x}$ expressed in its pseudovector form, *i.e.* $(x_{11}, x_{22}, x_{12})$ |
| $x^{(\mathrm{i})}$ | initial estimate of variable $x$ |
| @X | on the $X$-points of the grid |
| $\overset{\triangledown}{\boldsymbol{x}}$ | upper-convected time derivative of symmetric (rank 2) tensor $\boldsymbol{x}$ |

### A4 Notations related to the discretization on the E-grid

The *bar* notation refers to a spatial interpolation. If $\phi$ is a scalar field naturally defined on either T- or F-points of the grid (Fig. 2.b), then $\bar{\phi}$ refers to the value of $\phi$ interpolated onto F- or T-points, respectively. The average of the four surrounding points is used:

$$\begin{aligned}
\bar{\phi}_{i,j} &= 1/4(\phi_{i,j} + \phi_{i-1,j} + \phi_{i-1,j-1} + \phi_{i,j-1}) \quad \text{if } \phi \text{ @F} \quad \text{(@T)} \\
\bar{\phi}_{i,j} &= 1/4(\phi_{i+1,j+1} + \phi_{i,j+1} + \phi_{i,j} + \phi_{i+1,j}) \quad \text{if } \phi \text{ @T} \quad \text{(@F)}
\end{aligned} \tag{A1}$$

Similarly, $\bar{\phi}^{\gamma}$ refers to the interpolated value of $\phi$, defined on T- or F-points onto U- or V-points:

$$\begin{aligned}
\bar{\phi}^{U}_{i,j} &= 1/2(\phi_{i+1,j} + \phi_{i,j}) \quad \text{if } \phi \text{ @T} \quad \text{(@U)} \\
\bar{\phi}^{V}_{i,j} &= 1/2(\phi_{i,j+1} + \phi_{i,j}) \quad \text{if } \phi \text{ @T} \quad \text{(@V)} \\
\bar{\phi}^{U}_{i,j} &= 1/2(\phi_{i,j} + \phi_{i,j-1}) \quad \text{if } \phi \text{ @F} \quad \text{(@U)} \\
\bar{\phi}^{V}_{i,j} &= 1/2(\phi_{i,j} + \phi_{i-1,j}) \quad \text{if } \phi \text{ @F} \quad \text{(@V)}
\end{aligned} \tag{A2}$$

https://doi.org/10.5194/gmd-2023-231
Preprint. Discussion started: 10 January 2024



The *hat* notation $\hat{x}$ refers to the F-centric counterpart of $x$, $x$ being a prognostic scalar or tensor (rank 1 or 2) defined in the T-centric grid (mind that if $x$ is the element of a tensor, $\hat{x}$ is not necessarily defined on F-points). Example: $\hat{d}$ and $\hat{\sigma}_{11}$ are prognostic fields defined on F-points (natural location for $d$ and $\sigma_{11}$ on the C-grid is the T-point); similarly, $\hat{\sigma}_{12}$ is defined on T-points (natural location for $\sigma_{12}$ on the C-grid is the F-point).

https://doi.org/10.5194/gmd-2023-231
Preprint. Discussion started: 10 January 2024

Geoscientific Model Development
Discussions
Open Access
EGU

### A5 Table of symbols related to the numerical implementation

| Symbol | Definition | Units |
|---|---|---|
| $\Delta T$ | *big* time-step for the advection and the thermodynamics | [s] |
| $\Delta t$ | *small* time-step specific to BBM rheology (time-splitting) | [s] |
| $N_s$ | $\equiv \Delta T / \Delta t$, time-splitting parameter | [-] |
| $k$ | time-level index of time splitting ($1 \leq k \leq N_s$) | [-] |
| $A, h, d$ | ice concentration, thickness and damage of ice @T | [-], [m], [-] |
| $\bar{A}, \bar{h}$ | ice concentration and thickness interpolated @F | [-], [m] |
| $\hat{d}$ | damage of ice @F | [-] |
| $\dot{\boldsymbol{\varepsilon}} \equiv (\dot{\varepsilon}_{11}, \dot{\varepsilon}_{22}, \dot{\varepsilon}_{12})$ | strain-rate tensor (2×2) of the T-centric cell | [$s^{-1}$] |
| $\hat{\dot{\boldsymbol{\varepsilon}}} \equiv (\hat{\dot{\varepsilon}}_{11}, \hat{\dot{\varepsilon}}_{22}, \hat{\dot{\varepsilon}}_{12})$ | strain-rate tensor (2×2) of the F-centric cell | [$s^{-1}$] |
| $\boldsymbol{\sigma} \equiv (\sigma_{11}, \sigma_{22}, \sigma_{12})$ | internal stress tensor (2×2) of the T-centric cell | [Pa] |
| $\hat{\boldsymbol{\sigma}} \equiv (\hat{\sigma}_{11}, \hat{\sigma}_{22}, \hat{\sigma}_{12})$ | internal stress tensor (2×2) of the F-centric cell | [Pa] |
| $\bar{A}^U, \bar{A}^V$ | ice concentration interpolated @U and @V | [m] |
| $\bar{h}^U, \bar{h}^V$ | ice thickness interpolated @U and @V | [m] |
| $u, v$ | ice velocity at the $\Delta t$ level (@U and @V) | [m $s^{-1}$] |
| $\hat{u}, \hat{v}$ | ice velocity at the $\Delta t$ level (@V and @U) | [m $s^{-1}$] |
| $U, V$ | ice velocity at the $\Delta T$ level (@U and @V) | [m $s^{-1}$] |
| $\hat{U}, \hat{V}$ | ice velocity at the $\Delta T$ level (@V and @U) | [m $s^{-1}$] |
| $C_{Dw}$ | ice-ocean drag coefficient | [-] |
| $\tau_x, \tau_y$ | ice-ocean stress @U and @V | [Pa] |
| $\hat{\tau}_x, \hat{\tau}_y$ | ice-ocean stress @V and @U | [Pa] |
| $u_o, v_o$ | surface ocean current @U and @V | [m $s^{-1}$] |
| $\bar{u}_o, \bar{v}_o$ | surface ocean current interpolated @V and @U | [m $s^{-1}$] |
| $\bar{u}_o, \bar{v}_o$ | surface ocean current interpolated @V and @U | [m $s^{-1}$] |
| $\gamma_C$ | cross-nudging coefficient | [-] |
| $C_{Da}$ | ice-atmosphere drag coefficient | [-] |
| `e1t` | T-centered $\Delta x$ that connects 2 neighboring U-points | [m] |
| `e2t` | T-centered $\Delta y$ that connects 2 neighboring V-points | [m] |
| `e1f` | F-centered $\Delta x$ that connects 2 neighboring V-points | [m] |
| `e2f` | F-centered $\Delta y$ that connects 2 neighboring U-points | [m] |
| `e1u` | U-centered $\Delta x$ that connects 2 neighboring T-points | [m] |
| `e2u` | U-centered $\Delta y$ that connects 2 neighboring F-points | [m] |
| `e1v` | V-centered $\Delta x$ that connects 2 neighboring F-points | [m] |
| `e2v` | V-centered $\Delta y$ that connects 2 neighboring T-points | [m] |

https://doi.org/10.5194/gmd-2023-231
Preprint. Discussion started: 10 January 2024

Geoscientific Model Development Discussions
Open Access

# Appendix B: Algorithm and discretization

## B1 Algorithm

**Time-splitting loop** $(\Delta t)$ / for $k=1$ to $N_s$:

- compute elasticity $E,\hat{E}$ and viscous relaxation time $\lambda,\hat{\lambda}$ as a function of damage $d^k,\hat{d}^k$ and current sea-ice concentration $A,\bar{A}$ (Eq. B5, B6)
- compute the normal stress invariant of $\boldsymbol{\sigma}^k$ and $\hat{\boldsymbol{\sigma}}^k \rightarrow \sigma_I^k,\hat{\sigma}_I^k$ (Eq. B11)
- compute $P_{max},\hat{P}_{max}$ as a function of current sea-ice thickness $h,\bar{h}$ and concentration $A,\bar{A}$ (Eq. B7)
- compute $\tilde{P},\hat{\tilde{P}}$ as a function of $P_{max},\hat{P}_{max}$ and $\sigma_I,\hat{\sigma}_I$ (Eq. B8)
- compute the 3 components of each strain-rate tensor $\dot{\boldsymbol{\varepsilon}},\hat{\dot{\varepsilon}}$, based on sea-ice velocities at time-level $k$ (Eq. B1, B2, B3 & B4)
- initial prognostic estimate of the stress tensors at time-level $k+1 \rightarrow \boldsymbol{\sigma}^{(\mathrm{i})k+1}$ and $\hat{\boldsymbol{\sigma}}^{(\mathrm{i})k+1}$ (Eq. B10)
- apply cross-nudging between $\boldsymbol{\sigma}^{(\mathrm{i})k+1}$ and $\hat{\boldsymbol{\sigma}}^{(\mathrm{i})k+1}$ (Eq. 16):
- *Mohr-Coulomb* test on $\boldsymbol{\sigma}^{(\mathrm{i})k+1}$ and $\hat{\boldsymbol{\sigma}}^{(\mathrm{i})k+1}$
  - ⋆ compute the 2 invariants of $\boldsymbol{\sigma}^{(\mathrm{i})k+1}$ and $\hat{\boldsymbol{\sigma}}^{(\mathrm{i})k+1} \rightarrow \sigma_I^{(\mathrm{i})k+1},\sigma_{II}^{(\mathrm{i})k+1}$ and $\hat{\sigma}_I^{(\mathrm{i})k+1},\hat{\sigma}_{II}^{(\mathrm{i})k+1}$ (Eq. B11)
  - ⋆ compute $d_{crit}$ and $\hat{d}_{crit}$ based on $\sigma_I^{(\mathrm{i})k+1},\sigma_{II}^{(\mathrm{i})k+1}$ and $\hat{\sigma}_I^{(\mathrm{i})k+1},\hat{\sigma}_{II}^{(\mathrm{i})k+1}$ (Eq. B12)
- prognostic estimate of the stress tensors and damage at time-level $k+1 \rightarrow \boldsymbol{\sigma}^{k+1}$, $d^{k+1}$ and $\hat{\boldsymbol{\sigma}}^{k+1}$, $\hat{d}^{k+1}$
  - ⋆ where $0<d_{crit}<1$ and/or $0<\hat{d}_{crit}<1$ (overcritical stress state):
    → damage growth and stress adjustment (Eq. B13)
  - ⋆ elsewhere:
    → no damage growth and no stress adjustment (Eq. B14)
- compute the divergence of the vertically-integrated $\boldsymbol{\sigma}^{k+1}$ and $\hat{\boldsymbol{\sigma}}^{k+1}$ (Eq. B16 & B17)
- prognostic estimate of sea-ice velocity at time-level $k+1 \rightarrow u^{k+1},v^{k+1}$ and $\hat{u}^{k+1},\hat{v}^{k+1}$ (Eq. B19 & B18)

**NEMO (big) time-step** $(\Delta T)$:

- BBM rheology (*time-splitting loop* above)
- advection of generic SI3 prognostic tracers ($A$, $h$, etc) at T-points using $U,V$
- advection of $d$, $\sigma_{11}$, $\sigma_{22}$ and $\hat{\sigma}_{12}$ at T-points using $U,V$
- advection of $\hat{d}$, $\hat{\sigma}_{11}$, $\hat{\sigma}_{22}$ and $\sigma_{12}$ at F-points using $\hat{U},\hat{V}$
- healing of damage ($d$ and $\hat{d}$) (Eq.15)
- thermodynamics module of SI3 (update of $A$, $h$, etc)

https://doi.org/10.5194/gmd-2023-231
Preprint. Discussion started: 10 January 2024

Geoscientific Model Development Discussions

### B2 Update of internal stress tensor in the T- and F-centric worlds

#### B2.1 Divergence, shear and strain-rate tensor of ice velocity

Following Hunke and Dukowicz (2002), here is how the components of the strain rate of the sea-ice velocity vector are computed on the T- and F-centric grids, based on the finite-difference method.

⋄ Divergence rate ($\partial_x u + \partial_y v$):

$$
\begin{aligned}
D_{i,j} &= \frac{[\texttt{e2u}\;u]_{i,j} - [\texttt{e2u}\;u]_{i-1,j} + [\texttt{e1v}\;v]_{i,j} - [\texttt{e1v}\;v]_{i,j-1}}{[\texttt{e1t}\;\texttt{e2t}]_{i,j}} \quad (@\mathrm{T}),\\
\hat{D}_{i,j} &= \frac{[\texttt{e2v}\;\hat{u}]_{i+1,j} - [\texttt{e2v}\;\hat{u}]_{i,j} + [\texttt{e1u}\;\hat{v}]_{i,j+1} - [\texttt{e1u}\;\hat{v}]_{i,j}}{[\texttt{e1f}\;\texttt{e2f}]_{i,j}} \quad (@\mathrm{F}).
\end{aligned}
\tag{B1}
$$

⋄ Tension rate ($\partial_x u - \partial_y v$):

$$
\begin{aligned}
T_{i,j} &= \frac{\left([u/\texttt{e2u}]_{i,j} - [u/\texttt{e2u}]_{i-1,j}\right)[\texttt{e2t}^2]_{i,j} - \left([v/\texttt{e1v}]_{i,j} - [v/\texttt{e1v}]_{i,j-1}\right)[\texttt{e1t}^2]_{i,j}}{[\texttt{e1t}\;\texttt{e2t}]_{i,j}} \quad (@\mathrm{T}),\\
\hat{T}_{i,j} &= \frac{\left([\hat{u}/\texttt{e2v}]_{i+1,j} - [\hat{u}/\texttt{e2v}]_{i,j}\right)[\texttt{e2f}^2]_{i,j} - \left([\hat{v}/\texttt{e1u}]_{i,j+1} - [\hat{v}/\texttt{e1u}]_{i,j}\right)[\texttt{e1f}^2]_{i,j}}{[\texttt{e1f}\;\texttt{e2f}]_{i,j}} \quad (@\mathrm{F}).
\end{aligned}
\tag{B2}
$$

⋄ Shearing rate ($\partial_y u + \partial_x v$):

$$
\begin{aligned}
S_{i,j} &= \frac{\left([u/\texttt{e1u}]_{i,j+1} - [u/\texttt{e1u}]_{i,j}\right)[\texttt{e1f}^2]_{i,j} + \left([v/\texttt{e2v}]_{i+1,j} - [v/\texttt{e2v}]_{i,j}\right)[\texttt{e2f}^2]_{i,j}}{[\texttt{e1f}\;\texttt{e2f}]_{i,j}} \quad (@\mathrm{F}),\\
\hat{S}_{i,j} &= \frac{\left([\hat{u}/\texttt{e1v}]_{i,j} - [\hat{u}/\texttt{e1v}]_{i,j-1}\right)[\texttt{e1t}^2]_{i,j} + \left([\hat{v}/\texttt{e2u}]_{i,j} - [\hat{v}/\texttt{e2u}]_{i-1,j}\right)[\texttt{e2t}^2]_{i,j}}{[\texttt{e1t}\;\texttt{e2t}]_{i,j}} \quad (@\mathrm{T}).
\end{aligned}
\tag{B3}
$$

From which the 3 components of the 2D strain-rate tensors are obtained:

$$
\begin{aligned}
\begin{pmatrix} \dot{\varepsilon}_{11} \\ \dot{\varepsilon}_{22} \\ \dot{\varepsilon}_{12} \end{pmatrix}_{i,j} &= \frac{1}{2}\begin{pmatrix} D_{i,j} + T_{i,j} \\ D_{i,j} - T_{i,j} \\ \hat{S}_{i,j} \end{pmatrix} \quad (@\mathrm{T})\\
\begin{pmatrix} \hat{\dot{\varepsilon}}_{11} \\ \hat{\dot{\varepsilon}}_{22} \\ \dot{\varepsilon}_{12} \end{pmatrix}_{i,j} &= \frac{1}{2}\begin{pmatrix} \hat{D}_{i,j} + \hat{T}_{i,j} \\ \hat{D}_{i,j} - \hat{T}_{i,j} \\ S_{i,j} \end{pmatrix} \quad (@\mathrm{F})
\end{aligned}
\tag{B4}
$$

#### B2.2 Update of the stress tensors

⋄ Elasticity of damaged ice:

$$
\begin{aligned}
E &= E_0\left(1-d\right)\,e^{C(1-A)} \quad (@\mathrm{T})\\
\hat{E} &= E_0\left(1-\hat{d}\right)\,e^{C(1-\bar{A})} \quad (@\mathrm{F})
\end{aligned}
\tag{B5}
$$

https://doi.org/10.5194/gmd-2023-231
Preprint. Discussion started: 10 January 2024

Geoscientific Model Development
Discussions

◇ Viscous relaxation time of damaged ice:

$$\begin{aligned}
&\lambda = \lambda 0 \left[\left(1-d\right)\, e^{C(1-A)}\right]^{\beta-1} \quad (@\mathrm{T})\\
&\hat{\lambda} = \lambda 0 \left[\left(1-\hat{d}\right)\, e^{C(1-\bar{A})}\right]^{\beta-1} \quad (@\mathrm{F})
\end{aligned} \tag{B6}$$

◇ Ridging threshold:

$$\begin{aligned}
&P_{max} = P0\left[h/h_0\right]^{3/2}\, e^{C(1-A)} \quad (@\mathrm{T})\\
&\hat{P}_{max} = P0\left[\bar{h}/h_0\right]^{3/2}\, e^{C(1-\bar{A})} \quad (@\mathrm{F})
\end{aligned} \tag{B7}$$

◇ $\tilde{P}$ term:

$$\begin{aligned}
&\tilde{P} = \begin{cases} \dfrac{\sigma_I}{-P_{max}} & \text{for } \sigma_I < -P_{max} \\ -1 & \text{for } -P_{max} \le \sigma_I < 0 \\ 0 & \text{for } \sigma_I > 0 \end{cases} \quad (@\mathrm{T})\\
&\hat{\tilde{P}} = \begin{cases} \dfrac{\hat{\sigma}_I}{-\hat{P}_{max}} & \text{for } \hat{\sigma}_I < -\hat{P}_{max} \\ -1 & \text{for } -\hat{P}_{max} \le \hat{\sigma}_I < 0 \\ 0 & \text{for } \hat{\sigma}_I > 0 \end{cases} \quad (@\mathrm{F})
\end{aligned} \tag{B8}$$

◇ Multiplicator for stress update:

$$\begin{aligned}
&\Omega = \frac{\lambda}{\lambda + (1+\tilde{P})\Delta t} \quad (@\mathrm{T})\\
&\hat{\Omega} = \frac{\hat{\lambda}}{\hat{\lambda} + (1+\hat{\tilde{P}})\Delta t} \quad (@\mathrm{F})
\end{aligned} \tag{B9}$$

◇ Initial update of stress tensor:

$$\begin{aligned}
&\left.\begin{aligned}
\sigma_{11}^{(\mathrm{i})k+1} &= \Omega\left[E\,\Delta t\,\frac{1}{1-\nu^2}\,(\dot{\varepsilon}_{11}^{k} + \nu\,\dot{\varepsilon}_{22}^{k}) + \sigma_{11}^{k}\right]\\
\sigma_{22}^{(\mathrm{i})k+1} &= \Omega\left[E\,\Delta t\,\frac{1}{1-\nu^2}\,(\nu\,\dot{\varepsilon}_{11}^{k} + \dot{\varepsilon}_{22}^{k}) + \sigma_{22}^{k}\right]\\
\hat{\sigma}_{12}^{(\mathrm{i})k+1} &= \hat{\Omega}\left[\hat{E}\,\Delta t\,\frac{1-\nu}{1-\nu^2}\,\hat{\dot{\varepsilon}}_{12}^{k} + \hat{\sigma}_{12}^{k}\right]
\end{aligned}\right\} \quad (@\mathrm{T})\\
&\left.\begin{aligned}
\hat{\sigma}_{11}^{(\mathrm{i})k+1} &= \hat{\Omega}\left[\hat{E}\,\Delta t\,\frac{1}{1-\nu^2}\,(\hat{\dot{\varepsilon}}_{11}^{k} + \nu\,\hat{\dot{\varepsilon}}_{22}^{k}) + \hat{\sigma}_{11}^{k}\right]\\
\hat{\sigma}_{22}^{(\mathrm{i})k+1} &= \hat{\Omega}\left[\hat{E}\,\Delta t\,\frac{1}{1-\nu^2}\,(\nu\,\hat{\dot{\varepsilon}}_{11}^{k} + \hat{\dot{\varepsilon}}_{22}^{k}) + \hat{\sigma}_{22}^{k}\right]\\
\sigma_{12}^{(\mathrm{i})k+1} &= \Omega\left[E\,\Delta t\,\frac{1-\nu}{1-\nu^2}\,\dot{\varepsilon}_{12}^{k} + \sigma_{12}^{k}\right]
\end{aligned}\right\} \quad (@\mathrm{F})
\end{aligned} \tag{B10}$$

◇ Invariants of stress tensor:

$$\begin{aligned}
&\sigma_I = \frac{1}{2}(\sigma_{11}+\sigma_{22}), \quad \sigma_{II} = \sqrt{\left(\frac{\sigma_{11}-\sigma_{22}}{2}\right)^2 + \hat{\sigma}_{12}^2} \quad (@\mathrm{T})\\
&\hat{\sigma}_I = \frac{1}{2}(\hat{\sigma}_{11}+\hat{\sigma}_{22}), \quad \hat{\sigma}_{II} = \sqrt{\left(\frac{\hat{\sigma}_{11}-\hat{\sigma}_{22}}{2}\right)^2 + \sigma_{12}^2} \quad (@\mathrm{F})
\end{aligned} \tag{B11}$$

https://doi.org/10.5194/gmd-2023-231
Preprint. Discussion started: 10 January 2024

Geoscientific Model Development
Discussions

⋄ Damage increment:

$$
\begin{aligned}
d_{crit} &= \begin{cases} \dfrac{c}{\sigma_{II}^{(i)} + \mu\,\sigma_{I}^{(i)}} & \text{if } \sigma_I^{(i)} > -N \\[2ex] \dfrac{-N}{\sigma_I^{(i)}} & \text{otherwise} \end{cases} \qquad (@T) \\
\hat{d}_{crit} &= \begin{cases} \dfrac{c}{\hat{\sigma}_{II}^{(i)} + \mu\,\hat{\sigma}_{I}^{(i)}} & \text{if } \hat{\sigma}_I^{(i)} > -N \\[2ex] \dfrac{-N}{\hat{\sigma}_I^{(i)}} & \text{otherwise} \end{cases} \qquad (@F)
\end{aligned}
\tag{B12}
$$

⋄ Update of damage and stress tensors:

⋆ in regions where $0 < d_{crit} < 1$:

620

$$
\begin{aligned}
&\begin{aligned} d^{k+1} &= d^k + (1-d_{crit})(1-d^k)\ \Delta t/t_d \\ \underline{\boldsymbol{\sigma}}^{k+1} &= \underline{\boldsymbol{\sigma}}^{(i)k+1} - (1-d_{crit})\ \underline{\boldsymbol{\sigma}}^{(i)k+1}\ \Delta t/t_d \end{aligned} \quad \text{with } t_d = \Delta x\sqrt{\frac{2(1+\nu)\rho_i}{E}} \qquad (@T) \\
&\begin{aligned} \hat{d}^{k+1} &= \hat{d}^k + (1-\hat{d}_{crit})(1-\hat{d}^k)\ \Delta t/\hat{t}_d \\ \underline{\hat{\boldsymbol{\sigma}}}^{k+1} &= \underline{\hat{\boldsymbol{\sigma}}}^{(i)k+1} - (1-\hat{d}_{crit})\ \underline{\hat{\boldsymbol{\sigma}}}^{(i)k+1}\ \Delta t/\hat{t}_d \end{aligned} \quad \text{with } \hat{t}_d = \Delta x\sqrt{\frac{2(1+\nu)\rho_i}{\hat{E}}} \qquad (@F)
\end{aligned}
\tag{B13}
$$

⋆ elsewhere:

$$
\begin{aligned}
&\begin{aligned} d^{k+1} &= d^k \\ \underline{\boldsymbol{\sigma}}^{k+1} &= \underline{\boldsymbol{\sigma}}^{(i)k+1} \end{aligned} \qquad (@T) \\
&\begin{aligned} \hat{d}^{k+1} &= \hat{d}^k \\ \underline{\hat{\boldsymbol{\sigma}}}^{k+1} &= \underline{\hat{\boldsymbol{\sigma}}}^{(i)k+1} \end{aligned} \qquad (@F)
\end{aligned}
\tag{B14}
$$

### B3 Update of sea-ice velocity

As opposed to aEVP for which SI3 uses the scheme of Kimmritz et al. (2016, 2017), here we chose to solve the equation for
625 momentum (in both the T- and F-centric worlds) using the implicit scheme approach of Bouillon et al. (2009).

#### B3.1 Divergence of the vertically-integrated stress tensor

⋄ Definition:

$$
\begin{pmatrix} \Delta_x \\ \Delta_y \end{pmatrix} \equiv \begin{pmatrix} \dfrac{\partial(h\,\sigma_{11})}{\partial x} + \dfrac{\partial(h\,\sigma_{12})}{\partial y} \\[2ex] \dfrac{\partial(h\,\sigma_{22})}{\partial y} + \dfrac{\partial(h\,\sigma_{12})}{\partial x} \end{pmatrix}
\tag{B15}
$$

https://doi.org/10.5194/gmd-2023-231
Preprint. Discussion started: 10 January 2024




◇ Discretized in the T-centric cell:

$$\Delta_x^{k+1}\Big|_{i,j} = \frac{\left[\sigma_{11}^{k+1} h\,\mathtt{e2t}^2\right]_{i+1,j} - \left[\sigma_{11}^{k+1}\, h\,\mathtt{e2t}^2\right]_{i,j}}{\left[\mathtt{e1u}\,\mathtt{e2u}^2\right]_{i,j}} + \frac{\left[\sigma_{12}^{k+1}\bar{h}\,\mathtt{e1f}^2\right]_{i,j} - \left[\sigma_{12}^{k+1}\,\bar{h}\,\mathtt{e1f}^2\right]_{i,j-1}}{\left[\mathtt{e2u}\,\mathtt{e1u}^2\right]_{i,j}} \quad (@\mathrm{U})$$

$$\Delta_y^{k+1}\Big|_{i,j} = \frac{\left[\sigma_{22}^{k+1} h\,\mathtt{e1t}^2\right]_{i,j+1} - \left[\sigma_{22}^{k+1}\, h\,\mathtt{e1t}^2\right]_{i,j}}{\left[\mathtt{e2v}\,\mathtt{e1v}^2\right]_{i,j}} + \frac{\left[\sigma_{12}^{k+1}\hat{h}\,\mathtt{e2f}^2\right]_{i,j} - \left[\sigma_{12}^{k+1}\,\hat{h}\,\mathtt{e2f}^2\right]_{i-1,j}}{\left[\mathtt{e1v}\,\mathtt{e2v}^2\right]_{i,j}} \quad (@\mathrm{V}) \tag{B16}$$

◇ Discretized in the F-centric cell:

$$\hat{\Delta}_x^{k+1}\Big|_{i,j} = \frac{\left[\hat{\sigma}_{11}^{k+1}\bar{h}\,\mathtt{e2f}^2\right]_{i,j} - \left[\hat{\sigma}_{11}^{k+1}\,\bar{h}\,\mathtt{e2f}^2\right]_{i-1,j}}{\left[\mathtt{e1v}\,\mathtt{e2v}^2\right]_{i,j}} + \frac{\left[\hat{\sigma}_{12}^{k+1} h\,\mathtt{e1t}^2\right]_{i,j+1} - \left[\hat{\sigma}_{12}^{k+1}\, h\,\mathtt{e1t}^2\right]_{i,j}}{\left[\mathtt{e2v}\,\mathtt{e1v}^2\right]_{i,j}} \quad (@\mathrm{V})$$

$$\hat{\Delta}_y^{k+1}\Big|_{i,j} = \frac{\left[\hat{\sigma}_{22}^{k+1}\bar{h}\,\mathtt{e1f}^2\right]_{i,j} - \left[\hat{\sigma}_{22}^{k+1}\,\bar{h}\,\mathtt{e1f}^2\right]_{i,j-1}}{\left[\mathtt{e2u}\,\mathtt{e1u}^2\right]_{i,j}} + \frac{\left[\hat{\sigma}_{12}^{k+1} h\,\mathtt{e2t}^2\right]_{i+1,j} - \left[\hat{\sigma}_{12}^{k+1}\, h\,\mathtt{e2t}^2\right]_{i,j}}{\left[\mathtt{e1u}\,\mathtt{e2u}^2\right]_{i,j}} \quad (@\mathrm{U}) \tag{B17}$$

### B3.2 Update of sea-ice velocity

For clarity, we gather the contributions of the wind stress, the *Coriolis* term, and the SSH tilt vectors in a single vector term named $(R_x, R_y)$. Because these 3 terms do not present any particular challenge to express with respect to the existing implementation of aEVP. Note, however, that with the E-grid no spatial interpolation is needed to express the discretized *Coriolis* term.

Implicitness of the scheme is introduced through the use of sea-ice velocity at level $k+1$ in the estimate of the basal ice-water stress vector $(\tau_x, \tau_y)$:

$$\begin{aligned}
\tau_x &= Z_x^k\left(u_o^k - u^{k+1}\right) && \text{with:}\quad Z_x^k = \overline{A}^{u}\,\rho_w\,C_{Dw}\sqrt{\left(u_o^k - u^k\right)^2 + \left(\overline{v}_o^{u\,k} - \hat{v}^k\right)^2} \quad (@\mathrm{U})\\
\tau_y &= Z_y^k\left(v_o^k - v^{k+1}\right) && \text{with:}\quad Z_y^k = \overline{A}^{v}\,\rho_w\,C_{Dw}\sqrt{\left(\overline{u}_o^{v\,k} - \hat{u}^k\right)^2 + \left(v_o^k - v^k\right)^2} \quad (@\mathrm{V})\\
\hat{\tau}_x &= \hat{Z}_x^k\left(\overline{u}_o^{v\,k} - \hat{u}^{k+1}\right) && \text{with:}\quad \hat{Z}_x^k = \overline{A}^{v}\,\rho_w\,C_{Dw}\sqrt{\left(\overline{u}_o^{v\,k} - \hat{u}^k\right)^2 + \left(v_o^k - v^k\right)^2} \quad (@\mathrm{V})\\
\hat{\tau}_y &= \hat{Z}_y^k\left(\overline{v}_o^{u\,k} - \hat{v}^{k+1}\right) && \text{with:}\quad \hat{Z}_y^k = \overline{A}^{u}\,\rho_w\,C_{Dw}\sqrt{\left(u_o^k - u^k\right)^2 + \left(\overline{v}_o^{u\,k} - \hat{v}^k\right)^2} \quad (@\mathrm{U})
\end{aligned} \tag{B18}$$

https://doi.org/10.5194/gmd-2023-231
Preprint. Discussion started: 10 January 2024



Then, the discretized equation of momentum yields the expression of the 2 velocity components at time-level $k+1$:

$$
\begin{aligned}
u^{k+1} &= \frac{\frac{\rho_i \bar{h}^u}{\Delta t}\ u^k + Z_x\ u_o^k + \Delta_x^{k+1} + R_x^k}{\frac{\rho_i \bar{h}^u}{\Delta t}\ + Z_x} \quad (@\mathrm{U}) \\
v^{k+1} &= \frac{\frac{\rho_i \bar{h}^v}{\Delta t}\ v^k + Z_y\ v_o^k + \Delta_y^{k+1} + R_y^k}{\frac{\rho_i \bar{h}^v}{\Delta t}\ + Z_y} \quad (@\mathrm{V}) \\
\hat{u}^{k+1} &= \frac{\frac{\rho_i \bar{h}^v}{\Delta t}\ \hat{u}^k + \hat{Z}_x\ \bar{u}_o^{v\,k} + \hat{\Delta}_x^{k+1} + \hat{R}_x^k}{\frac{\rho_i \bar{h}^v}{\Delta t}\ + \hat{Z}_x} \quad (@\mathrm{V}) \\
\hat{v}^{k+1} &= \frac{\frac{\rho_i \bar{h}^u}{\Delta t}\ \hat{v}^k + \hat{Z}_y\ \bar{v}_o^{u\,k} + \hat{\Delta}_y^{k+1} + \hat{R}_y^k}{\frac{\rho_i \bar{h}^u}{\Delta t}\ + \hat{Z}_y} \quad (@\mathrm{U})
\end{aligned}
\tag{B19}
$$

# Appendix C: Model tuning & computation of sea-ice deformation rates

## C1 Model tuning

The value of the BBM-specific parameters used in the SI3-BBM simulation are presented in table A1.

## C2 Construction of the RGPS deformation rates and their simulated counterparts

The period of interest, chosen to match that of the production segment of the two simulations, *i.e.* December 15$^{\text{th}}$ 1996 to April 20$^{\text{th}}$ 1997 is divided into 3-day long bins, which corresponds to the nominal time resolution of the RGPS dataset.

### C2.1 Selection of RGPS point trajectories

As the first step of our selection process, for each 3-day bin, an initial subset of the RGPS points is selected. Each point of this initial subset must satisfy the following requirements:

- the point has at least one position that occurs within the time interval of the bin; this position, or the earliest-occurring one if more than one occurrence, is selected and referred to as position #1
- position #1 is located at least 100 km away from the nearest coastline
- the point has at least one upcoming position that occurs 3 days after position #1, with a tolerated deviation of ± 6 hours, referred to as position #2 (in the event of more than one position satisfying this requirement, the position yielding the time interval the closest to 3 days is selected)

### C2.2 Quadrangulation of selected trajectories

As the second step, a *Delaunay* triangulation is performed on this initial subset of points at position #1. Neighboring pairs of reasonably well shaped triangles are then merged into quadrangles in order to transform the triangular mesh into a quadrangular mesh.

https://doi.org/10.5194/gmd-2023-231
Preprint. Discussion started: 10 January 2024

Geoscientific Model Development
Discussions

*Aspiring quadrangles* at position #2 are constructed by simply considering the exact same respective sets of 4 points as those defining quadrangles at position #1.

Then, as the third and final step of the selection process, only points that define quadrangles that satisfy the following requirements, at both position #1 and position #2, are retained:

- the area of the quadrangle is consistent with the spatial scale of interest
- the time position of the four points defining the vertices of the quadrangle must be almost identical
- the thresholds for the minimum and maximum angles allowed are 40°and 140°, respectively

### C2.3 Computation of deformation rates based on the quadrangles

For all quadrangles selected in a given 3-day bin, strain-rates are computed based on position #1 and position #2 of the quadrangle, using the line-integral approximations (see *e.g.* Lindsay and Stern, 2003, equations 10-14).

Similarly to what is used as a $\Delta t$ to estimate velocities from displacements when computing the deformation rates, the actual time location (*i.e.* date) assigned to each deformation rate is not that of the center of the 3-day bin considered. Instead, we assign the time that corresponds to the center of the time interval defined by position #1 and position #2 of each quadrangle. Spatial location of the deformation rates corresponds to the barycenter of the 4 vertices of the quadrangle considered at the center of this same time interval.

### C2.4 Construction of the simulated *Lagrangian* sea-ice trajectories

To prevent computational waste, only the points from which valid RGPS deformation estimates were computed are retained. Each of these points is seeded using the same initialization date and location (bilinear interpolation) as its RGPS counterpart. It is then tracked during the same time interval of about 3 days (± 6 h) that separates the two consecutive records of the RGPS point considered. The tracking algorithm uses a time-step of 1 h and feeds on the hourly-averaged simulated sea-ice velocities of the SI3 experiments.

Only the conventional C-grid velocities $u, v$ of the T-centric cell are used to track the points ($\hat{u}, \hat{v}$ not used), which allows for the fair comparison between the two experiments, as no $\hat{u}, \hat{v}$ are available for SI3-aEVP.

*Author contributions.* This study was originally thought by P. Rampal and E. Ólason. The implementation of the BBM rheology into SI3 has been carried out by L. Brodeau, with the help of P. Rampal. E. Ólason suggested using the E-grid. The statistical analyses have been done by L. Brodeau, as well as all the figures. Interpretations of the results are from L. Brodeau, P. Rampal and E. Ólason. L. Brodeau and P. Rampal led the writing of the manuscript, with inputs from E. Ólason. Advice and various improvement suggestions have been provided by V. Dansereau.

https://doi.org/10.5194/gmd-2023-231
Preprint. Discussion started: 10 January 2024



*Competing interests.* The authors declare that the research was conducted in the absence of any commercial or financial relationships that could be construed as a potential conflict of interest

*Acknowledgements.* This study has been financially supported by the Schmidt Futures foundation (grant number 353) through the SASIP international project. Schmidt Futures is a philanthropic initiative founded by Eric and Wendy Schmidt that bets early on exceptional people making the world better, particularly through innovative breakthroughs in science and technology.

https://doi.org/10.5194/gmd-2023-231
Preprint. Discussion started: 10 January 2024


Geoscientific Model Development
Discussions

## References

Arakawa, A.: Design of the UCLA general circulation model, Tech. Rept. No. 7, 116 pp., University of California at Los Angeles, CA, 90024, 1972.

Arakawa, A. and Lamb, V. R.: Computational Design of the Basic Dynamical Processes of the UCLA General Circulation Model, in: Methods in Computational Physics: Advances in Research and Applications, pp. 173–265, https://doi.org/10.1016/b978-0-12-460817-7.50009-4, 1977.

Asselin, R.: Frequency Filter for Time Integrations, Monthly Weather Review, 100, 487–490, https://doi.org/10.1175/1520-0493(1972)100<0487:fffti>2.3.co;2, 1972.

Barnier, B., Madec, G., Penduff, T., Molines, J.-M., Treguier, A.-M., Sommer, J. L., Beckmann, A., Biastoch, A., Böning, C., Dengg, J., Derval, C., Durand, E., Gulev, S., Remy, E., Talandier, C., Theetten, S., Maltrud, M., McClean, J., and Cuevas, B. D.: Impact of partial steps and momentum advection schemes in a global ocean circulation model at eddy-permitting resolution, Ocean Dynamics, 56, 543–567, 2006.

Bouchat, A., Hutter, N., Chanut, J., Dupont, F., Dukhovskoy, D., Garric, G., Lee, Y., Lemieux, J.-F., Lique, C., Losch, M., Maslowski, W., Myers, P. G., Ólason, E., Rampal, P., Rasmussen, T., Talandier, C., Tremblay, B., and Wang, Q.: Sea Ice Rheology Experiment (SIREx), part I: Scaling and statistical properties of sea-ice deformation fields, Journal of Geophysical Research: Oceans, https://doi.org/10.1029/2021jc017667, 2022.

Bouillon, S., Maqueda, M. Á. M., Legat, V., and Fichefet, T.: An elastic–viscous–plastic sea ice model formulated on Arakawa B and C grids, Ocean Modelling, 27, 174–184, https://doi.org/10.1016/j.ocemod.2009.01.004, 2009.

Boutin, G., Ólason, E., Rampal, P., Regan, H., Lique, C., Talandier, C., Brodeau, L., and Ricker, R.: Arctic sea ice mass balance in a new coupled ice–ocean model using a brittle rheology framework, The Cryosphere, 17, 617–638, https://doi.org/10.5194/tc-17-617-2023, 2023.

Coon, M. D., Maykut, S. A., Pritchard, R. S., Rothrock, D. A., and Thorndike, A. S.: Modeling the pack ice as an elastic-plastic material, AIDJEX Bull., 24, 1–105, 1974.

Dansereau, V.: A Maxwell-Elasto-Brittle model for the drift and deformation of sea ice, Ph.D. thesis, Université Grenoble Alpes, 2016.

Dansereau, V., Weiss, J., Saramito, P., and Lattes, P.: A Maxwell elasto-brittle rheology for sea ice modelling, The Cryosphere, 10, 1339–1359, https://doi.org/10.5194/tc-10-1339-2016, 2016.

Dansereau, V., Weiss, J., Saramito, P., Lattes, P., and Coche, E.: Ice bridges and ridges in the Maxwell-EB sea ice rheology, The Cryosphere, 11, 2033–2058, https://doi.org/10.5194/tc-11-2033-2017, 2017.

Ferry, N., Barnier, B., Garric, G., Haines, K., Masina, S., Parent, L., Storto, A., Valdivieso, M., Guinehut, S., and Mulet, S.: NEMO: the modelling engine of global ocean reanalyses, Mercator Ocean Quarterly Newsletter, 46, 46–59, 2012.

Girard, L., Bouillon, S., Weiss, J., Amitrano, D., Fichefet, T., and Legat, V.: A new modeling framework for sea-ice mechanics based on elasto-brittle rheology, Annals of Glaciology, 52, 123–132, https://doi.org/10.3189/172756411795931499, 2011.

Hersbach, H., Bell, B., Berrisford, P., Hirahara, S., Horányi, A., Muñoz-Sabater, J., Nicolas, J., Peubey, C., Radu, R., Schepers, D., Simmons, A., Soci, C., Abdalla, S., Abellan, X., Balsamo, G., Bechtold, P., Biavati, G., Bidlot, J., Bonavita, M., Chiara, G., Dahlgren, P., Dee, D., Diamantakis, M., Dragani, R., Flemming, J., Forbes, R., Fuentes, M., Geer, A., Haimberger, L., Healy, S., Hogan, R. J., Hólm, E., Janisková, M., Keeley, S., Laloyaux, P., Lopez, P., Lupu, C., Radnoti, G., Rosnay, P., Rozum, I., Vamborg, F., Villaume, S., and Thépaut, J.-

https://doi.org/10.5194/gmd-2023-231
Preprint. Discussion started: 10 January 2024


Geoscientific Model Development Discussions

N.: The ERA5 global reanalysis, Quarterly Journal of the Royal Meteorological Society, 146, 1999–2049, https://doi.org/10.1002/qj.3803, 2020.

Hunke, E., Lipscomb, W., Jones, P., Turner, A., Jeffery, N., and Elliott, S.: CICE, The Los Alamos Sea Ice Model, Version 00, https://www.osti.gov//servlets/purl/1364126, 2017.

Hunke, E. C. and Dukowicz, J. K.: The Elastic–Viscous–Plastic Sea Ice Dynamics Model in General Orthogonal Curvilinear Coordinates on a Sphere—Incorporation of Metric Terms, Monthly Weather Review, 130, 1848–1865, https://doi.org/10.1175/1520-0493(2002)130<1848:tevpsi>2.0.co;2, 2002.

Hutter, N., Bouchat, A., Dupont, F., Dukhovskoy, D., Koldunov, N., Lee, Y. J., Lemieux, J.-F., Lique, C., Losch, M., Maslowski, W., Myers, P. G., Ólason, E., Rampal, P., Rasmussen, T., Talandier, C., Tremblay, B., and Wang, Q.: Sea Ice Rheology Experiment (SIREx): 2. Evaluating Linear Kinematic Features in High-Resolution Sea Ice Simulations, Journal of Geophysical Research: Oceans, 127, https://doi.org/10.1029/2021jc017666, 2022.

IPCC: The Ocean and Cryosphere in a Changing Climate: Special Report of the Intergovernmental Panel on Climate Change, pp. 203–320, Cambridge University Press, https://doi.org/10.1017/9781009157964.005, 2022.

Janjić, Z. I.: A Stable Centered Difference Scheme Free of Two-Grid-Interval Noise, Monthly Weather Review, 102, 319–323, https://doi.org/https://doi.org/10.1175/1520-0493(1974)102<0319:ASCDSF>2.0.CO;2, 1974.

Janjić, Z. I.: Nonlinear Advection Schemes and Energy Cascade on Semi-Staggered Grids, Monthly Weather Review, 112, 1234–1245, https://doi.org/10.1175/1520-0493(1984)112<1234:nasaec>2.0.co;2, 1984.

Janjić, Z. I. and Mesinger, F.: Finite-difference schemes for the shallow water equations on various horizontal grids, Ph.D. thesis, ECMWF, Shinfield Park, Reading, 1983.

Kagan, Y. Y. and Jackson, D. D.: Long-Term Earthquake Clustering, Geophysical Journal International, 104, 117–134, https://doi.org/10.1111/j.1365-246x.1991.tb02498.x, 1991.

Kimmritz, M., Danilov, S., and Losch, M.: The adaptive EVP method for solving the sea ice momentum equation, Ocean Modelling, 101, 59–67, https://doi.org/10.1016/j.ocemod.2016.03.004, 2016.

Kimmritz, M., Losch, M., and Danilov, S.: A comparison of viscous-plastic sea ice solvers with and without replacement pressure, Ocean Modelling, 115, 59–69, https://doi.org/10.1016/j.ocemod.2017.05.006, 2017.

Konor, C. S. and Randall, D. A.: Impacts of the horizontal and vertical grids on the numerical solutions of the dynamical equations – Part 1: Nonhydrostatic inertia–gravity modes, Geoscientific Model Development, 11, 1753–1784, https://doi.org/10.5194/gmd-11-1753-2018, 2018.

Kwok, R., Schweiger, A., Rothrock, D. A., Pang, S., and Kottmeier, C.: Sea ice motion from satellite passive microwave imagery assessed with ERS SAR and buoy motions, Journal of Geophysical Research: Oceans, 103, 8191–8214, https://doi.org/10.1029/97jc03334, 1998.

Lemieux, J., Tremblay, B., Thomas, S., Sedláček, J., and Mysak, L. A.: Using the preconditioned Generalized Minimum RESidual (GMRES) method to solve the sea-ice momentum equation, Journal of Geophysical Research: Oceans (1978–2012), 113, C10 004, https://doi.org/10.1029/2007jc004680, 2008.

Lemieux, J.-F., Knoll, D. A., Losch, M., and Girard, C.: A second-order accurate in time IMplicit–EXplicit (IMEX) integration scheme for sea ice dynamics, Journal of Computational Physics, 263, 375–392, https://doi.org/https://doi.org/10.1016/j.jcp.2014.01.010, 2014.

Lindsay, R. W. and Stern, H. L.: The RADARSAT Geophysical Processor System: Quality of Sea Ice Trajectory and Deformation Estimates, Journal of Atmospheric and Oceanic Technology, 20, 1333–1347, https://doi.org/10.1175/1520-0426(2003)020<1333:trgpsq>2.0.co;2, 2003.

https://doi.org/10.5194/gmd-2023-231
Preprint. Discussion started: 10 January 2024

Geoscientific Model Development Discussions

Losch, M., Menemenlis, D., Campin, J.-M., Heimbach, P., and Hill, C.: On the formulation of sea-ice models. Part 1: Effects of different solver implementations and parameterizations, Ocean Modelling, 33, 129–144, https://doi.org/10.1016/j.ocemod.2009.12.008, 2010.

Lovejoy, S. and Schertzer, D.: Nonlinear Dynamics in Geosciences, vol. 59 of *Nonlinear Dynamics in Geosciences*, pp. 311–337, ISBN 9780387349176, https://doi.org/10.1007/978-0-387-34918-3_18, 2007.

Madec, G., Bourdallé-Badie, R., Chanut, J., Clementi, E., Coward, A., Ethé, C., Iovino, D., Lea, D., Lévy, C., Lovato, T., Martin, N., Masson, S., Mocavero, S., Rousset, C., Storkey, D., Müeller, S., Nurser, G., Bell, M., Samson, G., Mathiot, P., Mele, F., and Moulin, A.: NEMO ocean engine, Zenodo, https://doi.org/10.5281/zenodo.1464816, 2022.

Marsaleix, P., Auclair, F., Duhaut, T., Estournel, C., Nguyen, C., and Ulses, C.: Alternatives to the Robert–Asselin filter, Ocean Modelling, 41, 53–66, https://doi.org/10.1016/j.ocemod.2011.11.002, 2012.

Marsan, D. and Weiss, J.: Space/time coupling in brittle deformation at geophysical scales, Earth and Planetary Science Letters, 296, 353 – 359, https://doi.org/10.1016/j.epsl.2010.05.019, 2010.

Marsan, D., Stern, H., Lindsay, R., and Weiss, J.: Scale dependence and localization of the deformation of arctic sea ice, Physical Review Letters, 93, 178 501, https://doi.org/10.1103/physrevlett.93.178501, 2004.

Mélia, D. S.: A global coupled sea ice–ocean model, Ocean Modelling, 4, 137–172, https://doi.org/10.1016/s1463-5003(01)00015-4, 2002.

Mesinger, F.: A method for construction of second-order accuracy difference schemes permitting no false two-grid-interval wave in the height field, Tellus, 25, 444–458, https://doi.org/https://doi.org/10.1111/j.2153-3490.1973.tb00629.x, 1973.

Mesinger, F. and Popovic, J.: Forward–backward scheme on the B/E grid modified to suppress lattice separation: the two versions, and any impact of the choice made?, Meteorology and Atmospheric Physics, 108, 1–8, https://doi.org/10.1007/s00703-010-0080-1, 2010.

Ólason, E., Boutin, G., Korosov, A., Rampal, P., Williams, T., Kimmritz, M., Dansereau, V., and Samaké, A.: A new brittle rheology and numerical framework for large-scale sea-ice models, Journal of Advances in Modeling Earth Systems, https://doi.org/10.1002/essoar.10507977.3, 2022.

Plante, M., Tremblay, B., Losch, M., and Lemieux, J.-F.: Landfast sea ice material properties derived from ice bridge simulations using the Maxwell elasto-brittle rheology, The Cryosphere, 14, 2137–2157, https://doi.org/10.5194/tc-14-2137-2020, 2020.

Prather, M. J.: Numerical advection by conservation of second-order moments, Journal of Geophysical Research, 91, 6671, https://doi.org/10.1029/jd091id06p06671, 1986.

Rampal, P., Weiss, J., Marsan, D., Lindsay, R., and Stern, H.: Scaling properties of sea ice deformation from buoy dispersion analysis, Journal of Geophysical Research, 113, https://doi.org/10.1029/2007jc004143, 2008.

Rampal, P., Bouillon, S., Ólason, E., and Morlighem, M.: neXtSIM: a new Lagrangian sea ice model, The Cryosphere, 10, 1055–1073, https://doi.org/10.5194/tc-10-1055-2016, 2016.

Rampal, P., Dansereau, V., Ólason, E., Bouillon, S., Williams, T., Korosov, A., and Samaké, A.: On the multi-fractal scaling properties of sea ice deformation, The Cryosphere, 13, 2457–2474, https://doi.org/10.5194/tc-13-2457-2019, 2019.

Rousset, C., Vancoppenolle, M., Madec, G., Fichefet, T., Flavoni, S., Barthélemy, A., Benshila, R., Chanut, J., Levy, C., Masson, S., and Vivier, F.: The Louvain-La-Neuve sea ice model LIM3.6: global and regional capabilities, Geoscientific Model Development, 8, 2991–3005, https://doi.org/10.5194/gmd-8-2991-2015, 2015.

Schertzer, D. and Lovejoy, S.: Physical modeling and analysis of rain and clouds by anisotropic scaling multiplicative processes, Journal of Geophysical Research: Atmospheres, 92, 9693–9714, https://doi.org/10.1029/jd092id08p09693, 1987.

Sornette, D.: Power Law Distributions, pp. 93–121, Springer Berlin Heidelberg, Berlin, Heidelberg, ISBN 978-3-540-33182-7, https://doi.org/10.1007/3-540-33182-4_4, 2006.

https://doi.org/10.5194/gmd-2023-231
Preprint. Discussion started: 10 January 2024

Geoscientific Model Development Discussions

Stern, H. L., Schweiger, A. J., Stark, M., Zhang, J., Steele, M., and Hwang, B.: Seasonal evolution of the sea-ice floe size distribution in the Beaufort and Chukchi seas, Elementa: Science of the Anthropocene, 6, 48, https://doi.org/10.1525/elementa.305, 2018.

Taylor, P., Hegyi, B., Boeke, R., and Boisvert, L.: On the Increasing Importance of Air-Sea Exchanges in a Thawing Arctic: A Review, Atmosphere, 9, https://doi.org/10.3390/atmos9020041, 2018.

Tremblay, L.-B. and Mysak, L. A.: Modeling sea ice as a granular material, including the dilatancy effect, Journal of Physical Oceanography, 27, 2342–2360, https://doi.org/10.1175/1520-0485(1997)027<2342:msiaag>2.0.co;2, 1997.

Vancoppenolle, M., Rousset, C., Blockley, E., Aksenov, Y., Feltham, D., Fichefet, T., Garric, G., Guémas, V., Iovino, D., Keeley, S., Madec, G., Massonnet, F., Ridley, J., Schroeder, D., and Tietsche, S.: SI3, the NEMO Sea Ice Engine, https://doi.org/10.5281/ZENODO.7534900, 2023.

Vihma, T.: Effects of Arctic Sea Ice Decline on Weather and Climate: A Review, Surveys in Geophysics, 35, 1175 – 1214, https://doi.org/10.1007/s10712-014-9284-0, 2014.

Weiss, J. and Dansereau, V.: Linking scales in sea ice mechanics, Philosophical Transactions of the Royal Society A: Mathematical, Physical and Engineering Sciences, 375, https://doi.org/10.1098/rsta.2015.0352, 2017.

Weiss, J., Marsan, D., and Rampal, P.: Space and time scaling laws induced by the multiscale fracturing of the Arctic sea ice cover, IUTAM Symposium on scaling in solid mechanics, 10, https://doi.org/10.1007/978-1-4020-9033-2, 2009.

https://doi.org/10.5194/gmd-2023-231
Preprint. Discussion started: 10 January 2024




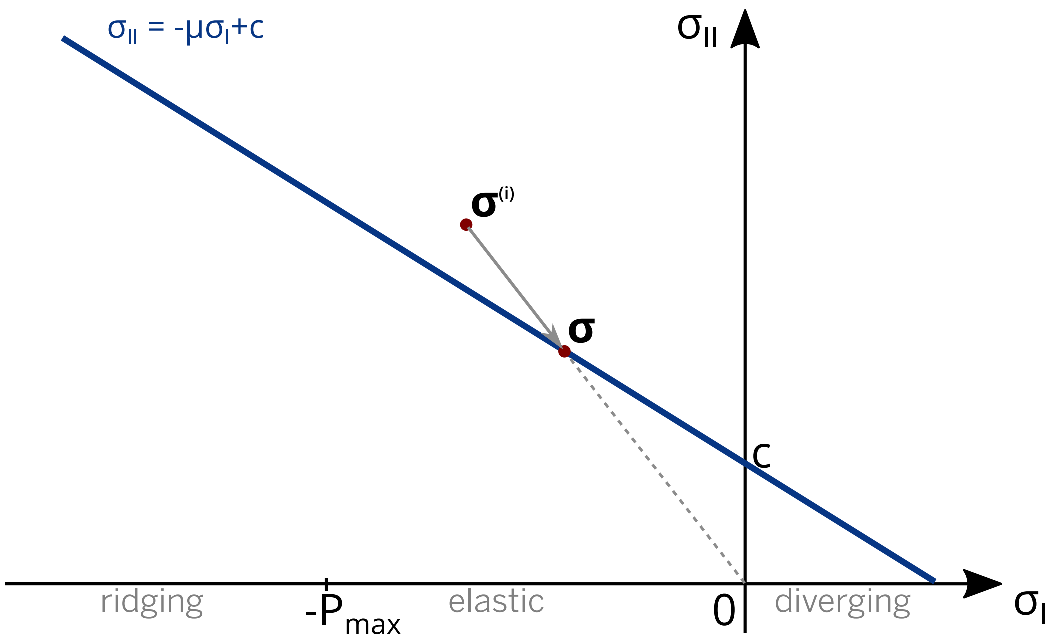


**Figure 1.** *Mohr-Coulomb* yield envelope in the internal stress invariant coordinates (blue line). Illustration of how an over-critical stress state $\boldsymbol{\sigma}^{(\mathrm{i})}$ (initial estimate) is evolving (gray arrow) towards the corrected state $\boldsymbol{\sigma}$ when using the BBM rheology.

https://doi.org/10.5194/gmd-2023-231
Preprint. Discussion started: 10 January 2024


Geoscientific Model Development
Discussions

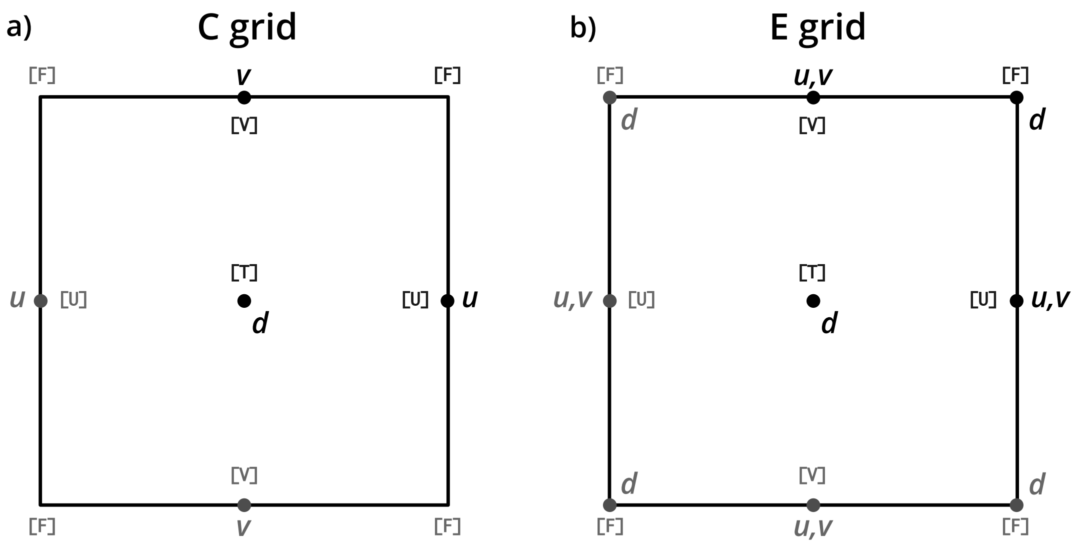


**Figure 2.** Point arrangement and staggering in a grid cell: (a) the C-grid as used in NEMO, and (b) the E-grid. The letter $d$ indicates the location of tracers, while letters $u$ and $v$ that of the $i$- and $j$-wise components of the velocity vector. Letters in brackets indicate the name of the grid points as referred to throughout the paper.

https://doi.org/10.5194/gmd-2023-231
Preprint. Discussion started: 10 January 2024


Geoscientific Model Development
Discussions
Open Access
EGU

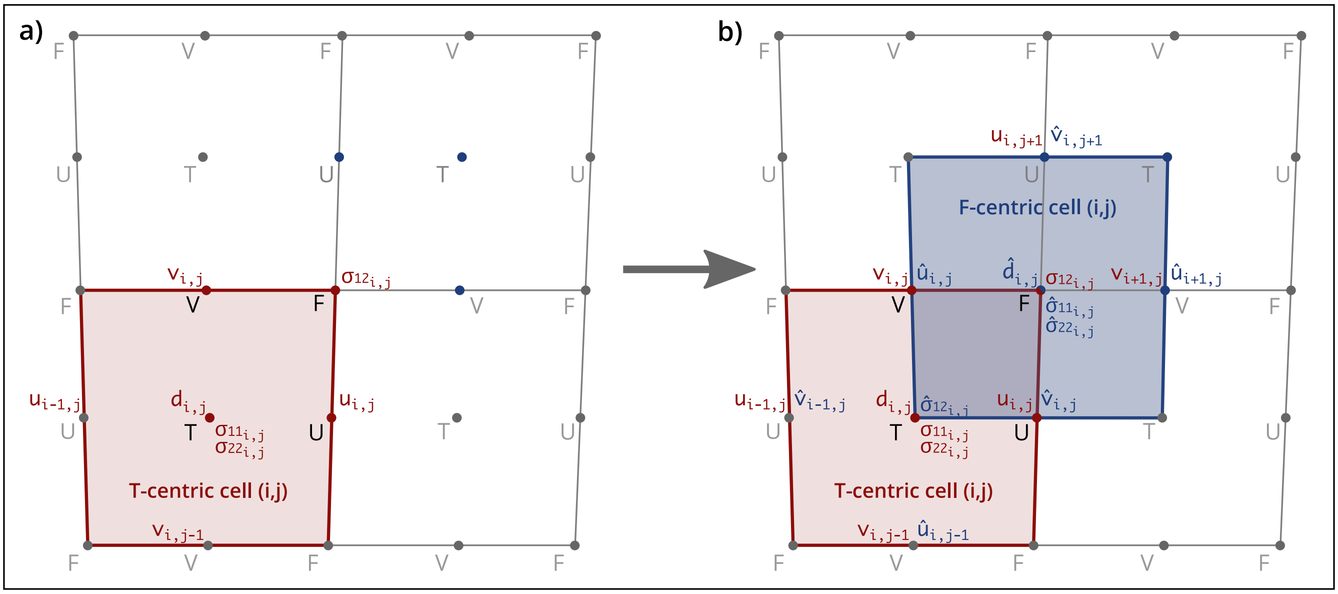

**Figure 3.** Transition from (a) the conventional C-grid staggering as used in NEMO to (b) the E-grid staggering proposed in this study. T-centric (red) and F-centric (blue) cells. $d$ is the damage tracer, $u$ and $v$ are the $i$- and $j$-wise components of the sea-ice velocity vector, and $\sigma_{kl}$ are the components of the internal stress tensor. The $\hat{x}$ notation indicates that variable $x$ is specific to the F-centric grid. Note: the F-centric counterparts of $u_{i,j}, v_{i,j}$ of the T-centric cell are $\hat{u}_{i+1,j}, \hat{v}_{i,j+1}$.

https://doi.org/10.5194/gmd-2023-231
Preprint. Discussion started: 10 January 2024


Geoscientific Model Development Discussions

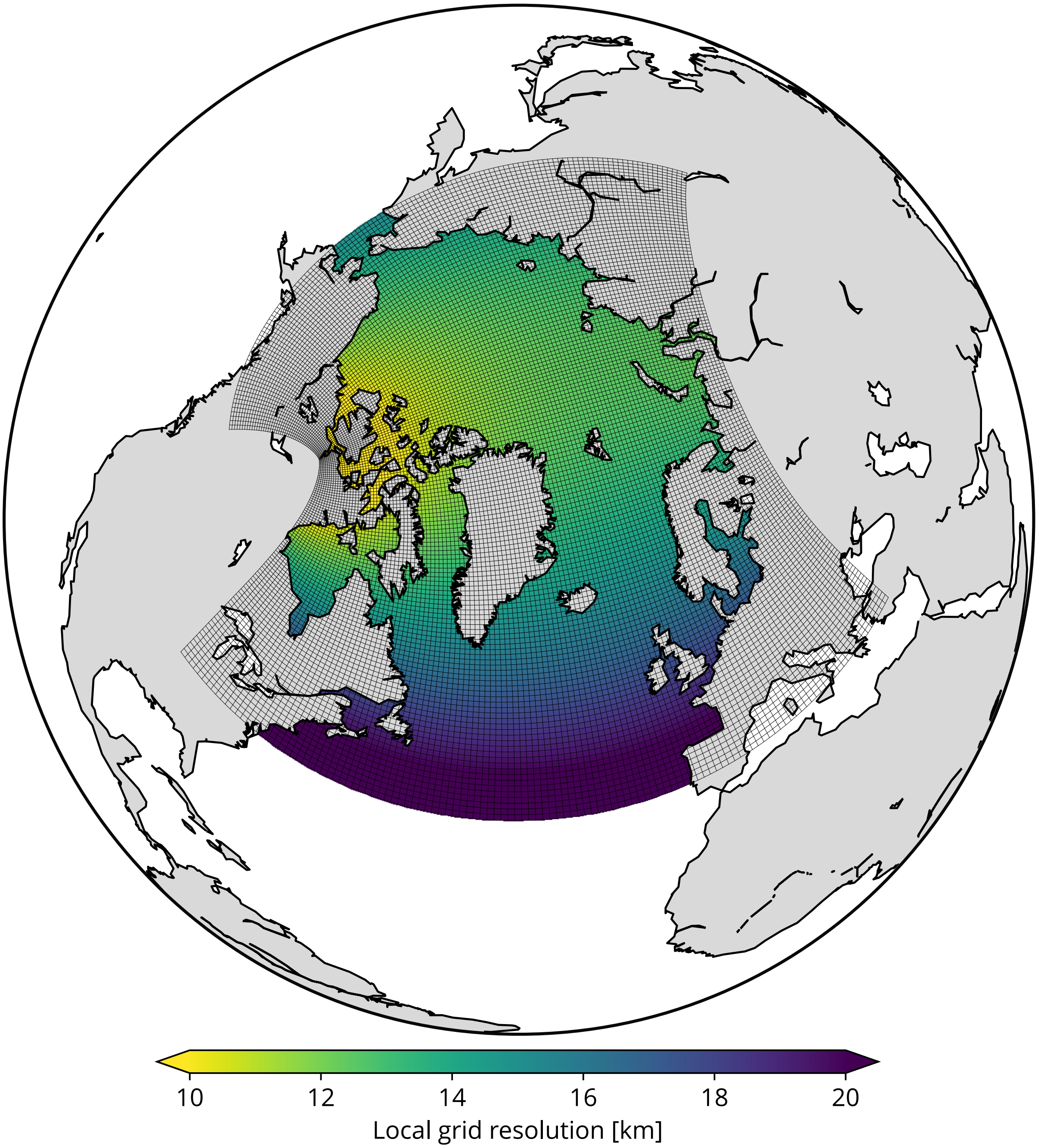


**Figure 4.** Geographical extent, numerical grid, and actual local spatial resolution of the NANUK4 computational domain that is used in the experiments. For ease of visual representation of the grid cells, grid points have been subsampled by a factor of 4.

https://doi.org/10.5194/gmd-2023-231
Preprint. Discussion started: 10 January 2024

Geoscientific Model Development
Discussions
Open Access

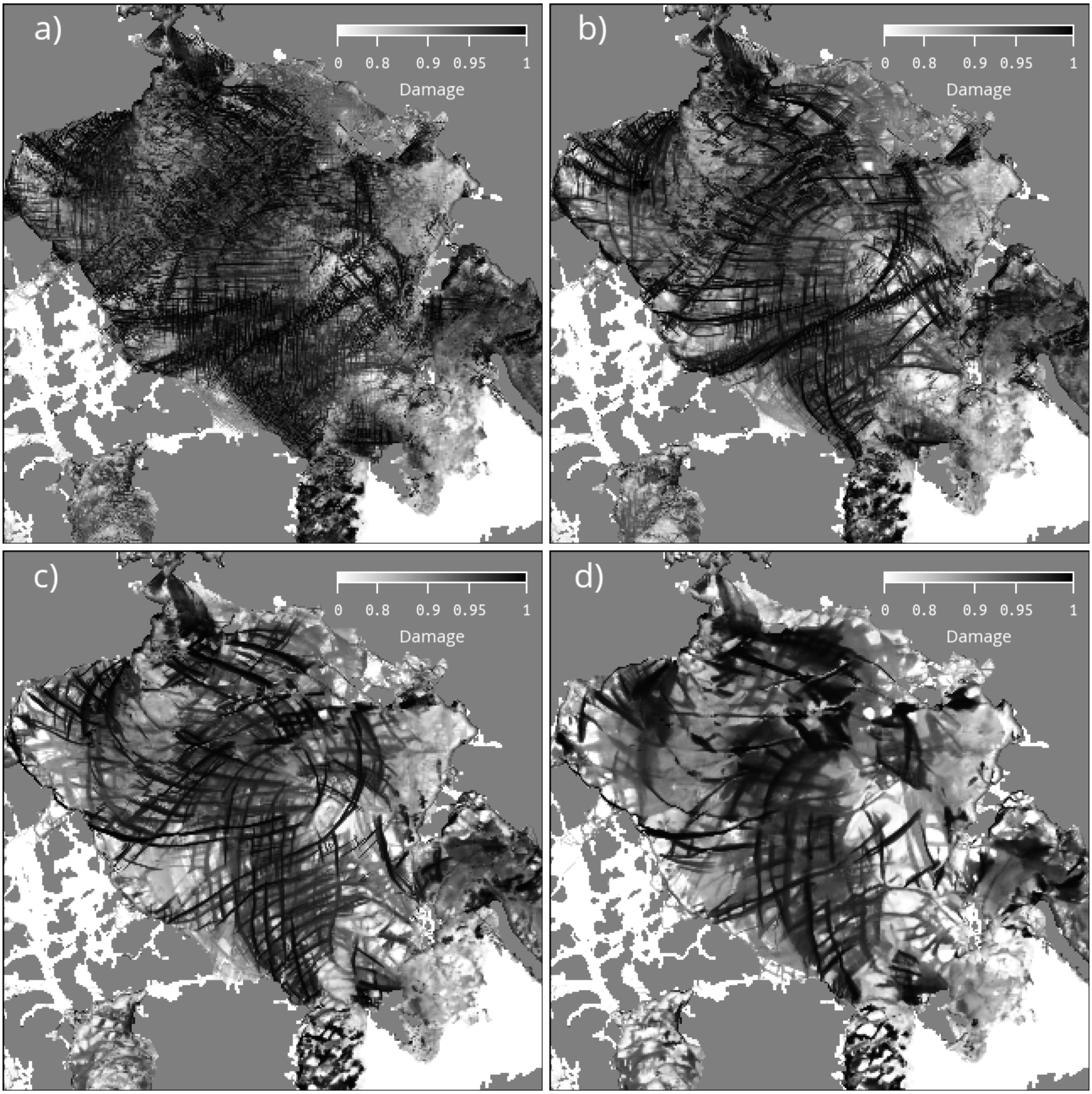


**Figure 5.** Effect of using different values for the cross-nudging coefficient $\gamma$ on the simulated sea-ice damage. Random snapshot of damage (at T-points) after 30 days of simulation (January 13th 1997) in a set of sensitivity experiments identical to SI3-BBM: (a) no cross-nudging , (b) $\gamma = 0.1$, (c) $\gamma = 2$ as in SI3-BBM, and (d) $\gamma = 10$.

https://doi.org/10.5194/gmd-2023-231
Preprint. Discussion started: 10 January 2024

Geoscientific Model Development Discussions
Open Access

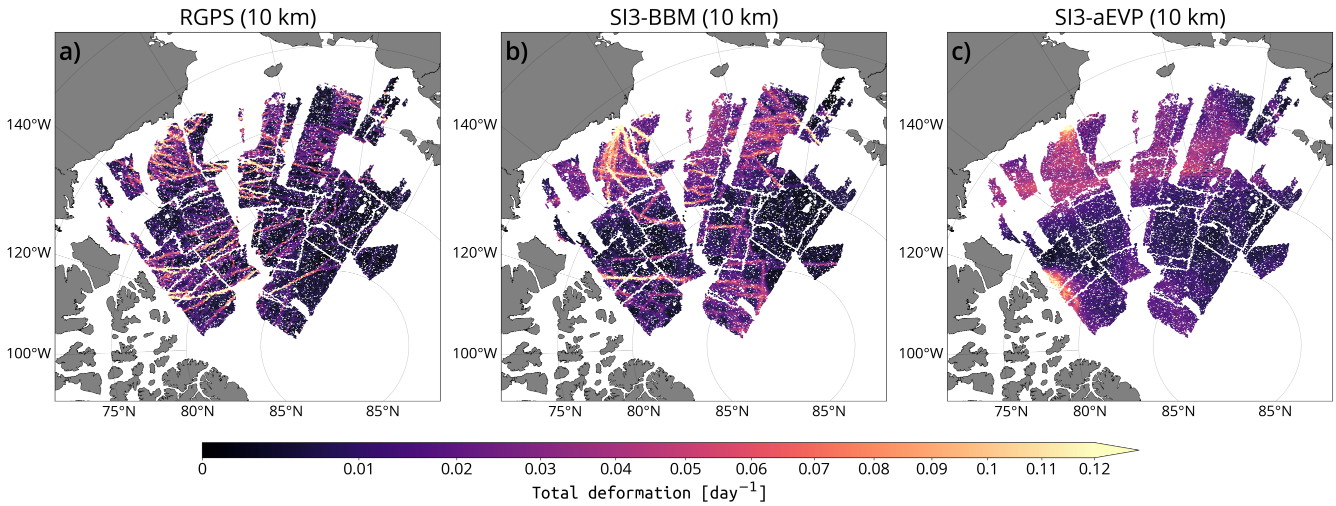


**Figure 6.** Maps of the sea-ice total deformation rate for the 3-day time window centered about the February 19th 1997, computed based on (a) RGPS *Lagrangian* data and (b,c) their synthetic counterparts constructed using the simulated sea-ice velocities of SI3-BBM an SI3-aEVP, respectively. Empty regions correspond to where satellite observations are not available over this particular 3-day time window.

https://doi.org/10.5194/gmd-2023-231
Preprint. Discussion started: 10 January 2024

Geoscientific Model Development
Discussions

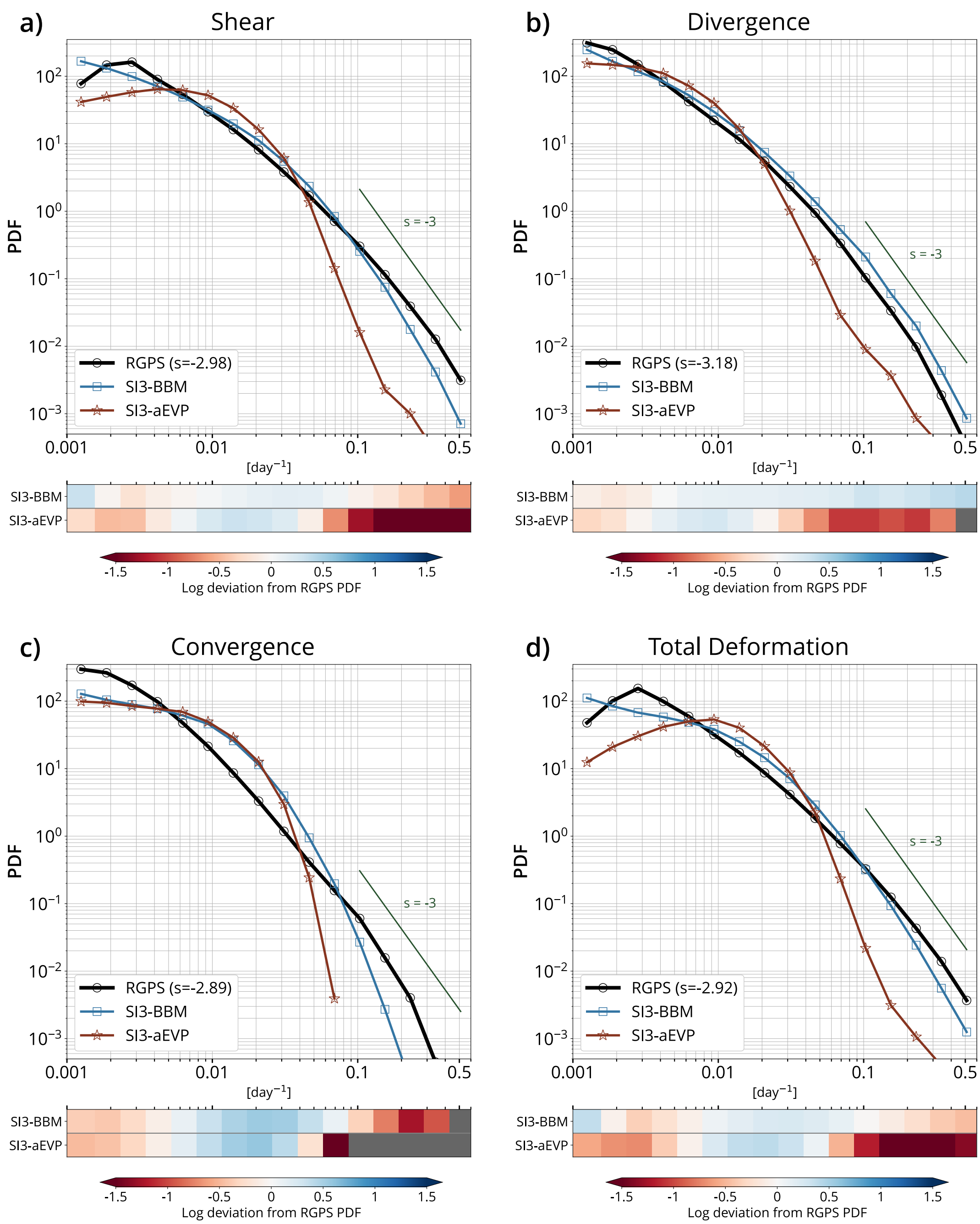


**Figure 7.** PDFs of the (a) shear, (b) divergence, (c) convergence, and (d) total deformation rates at the 10 km spatial and 3-day temporal scale, for RGPS data and their synthetic counterparts constructed using the simulated sea-ice velocities of SI3-BBM an SI3-aEVP. The light gray lines are for reference and correspond to a power-law with an exponent of -3. Below each panel, the departure between the logarithm of the simulated and observed distributions is shown for each bin.

https://doi.org/10.5194/gmd-2023-231
Preprint. Discussion started: 10 January 2024


Geoscientific Model Development
Discussions

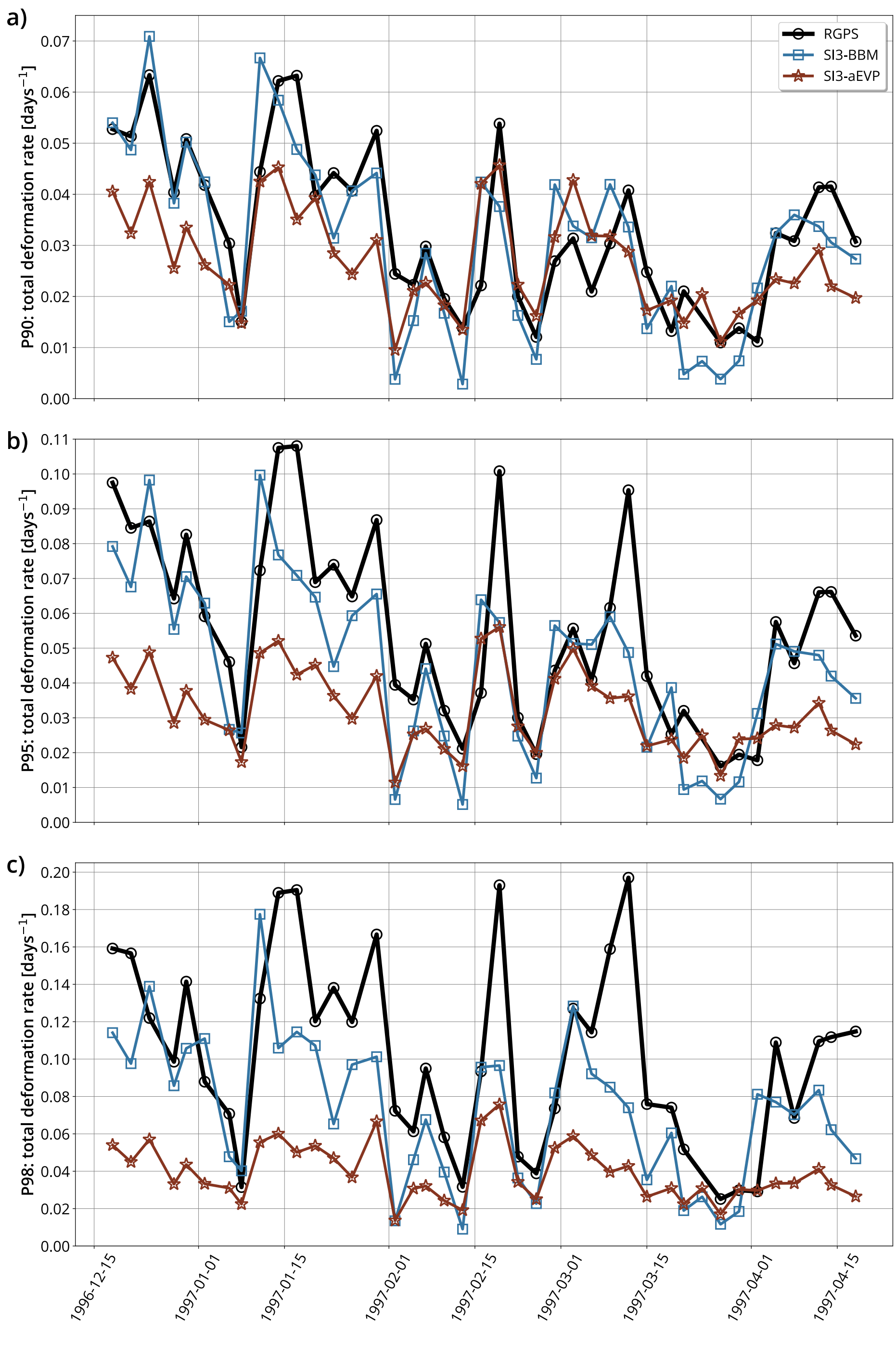


**Figure 8.** Time-series of the a) 90, b) 95, and c) 98 percentiles of the sea-ice total deformation rate for winter 1996-1997, at the 10 km spatial and 3-day temporal scale, for RGPS data and and their synthetic counterparts constructed using the simulated sea-ice velocities of SI3-BBM an SI3-aEVP.

https://doi.org/10.5194/gmd-2023-231
Preprint. Discussion started: 10 January 2024


Geoscientific Model Development
Discussions

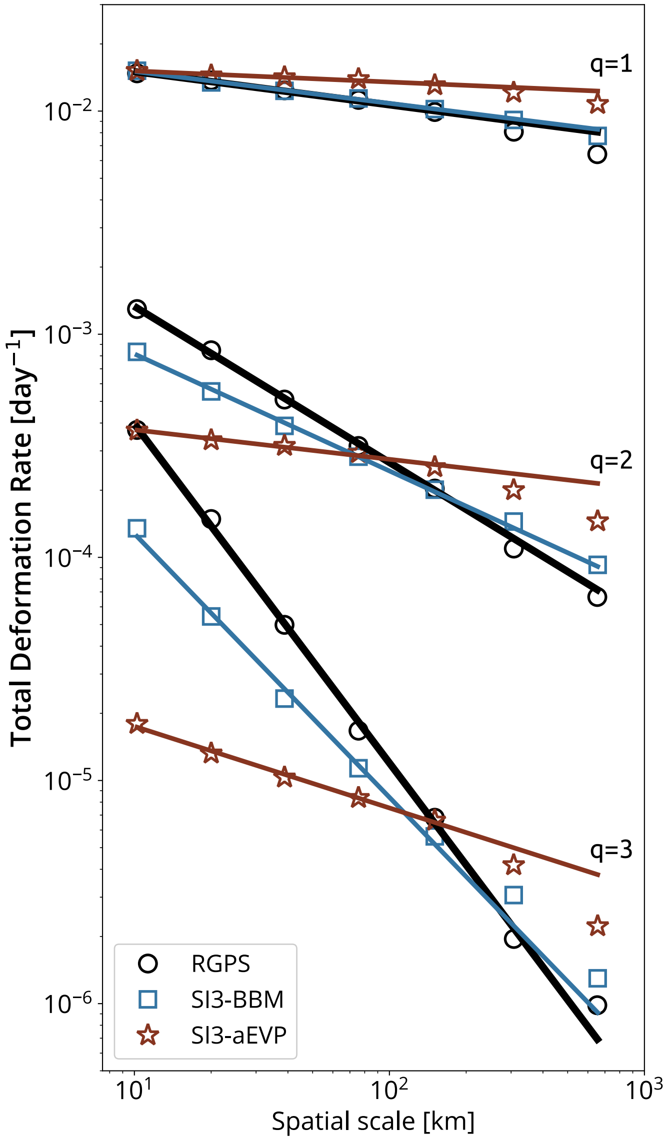


**Figure 9.** Spatial scaling analysis of the observed and simulated total deformation rate calculated over a 3-day time scale (all based on the motion of the same RGPS quadrangles) , based on RGPS data and their synthetic counterparts constructed using the simulated sea-ice velocities of SI3-BBM an SI3-aEVP. Moments of order $q = 1,2,3$ of the distributions of the total deformation rate calculated at scales spanning 10 up to 640 km. The solid straight lines indicate the associated power-law scaling based on the least-square fit using values from 10 km to 160 km. Values for 320 km and 640 km are excluded due to excessive uncertainty resulting from the small sample size. Note: we used logarithmically spaced bins and applied an ordinary least square method to the binned data in log-log space to get reasonably accurate estimate of these power-law fits (Stern et al., 2018).

https://doi.org/10.5194/gmd-2023-231
Preprint. Discussion started: 10 January 2024


Geoscientific Model Development
Discussions

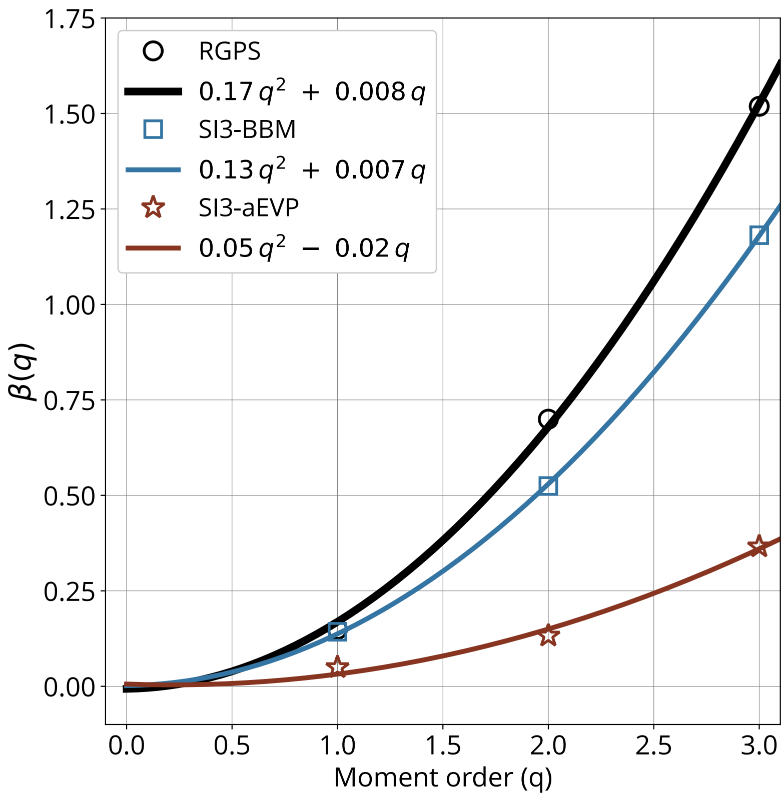


**Figure 10.** Structure functions $\beta(q)$ for the RGPS data (black), SI3-BBM (blue), and SI3-aEVP (red), where $\beta$ indicates the exponent of the power-law fits indicated in figure 9 and $q$ is the moment order.

https://doi.org/10.5194/gmd-2023-231
Preprint. Discussion started: 10 January 2024

Geoscientific Model Development
Discussions

**Table 1.** Summary of the differences in tuning options between the two experiments and the default in SI3.

| | **SI3-BBM** | **SI3-aEVP** | **Default in SI3** |
|---|---|---|---|
| Rheology | BBM | aEVP | aEVP |
| Ice-atm. drag coefficient $C_{Da}$ | 1.65 $10^{-3}$ | 1.15 $10^{-3}$ | 1.4 $10^{-3}$ |
| Subcycles of $\Delta T$ | 180 (time-splitting) | 180 (iterations) | 100 (iterations) |

**Table 2.** Bias, RMSE and *Pearson* correlation of the deformation rates time-series of figure 8 obtained between each simulation and RGPS.

| | **Experiment** | **Bias** | **Error** | **$\rho$ (p-value)** |
|---|---|---|---|---|
| P90 | SI3-BBM | -0.002 | 0.01 | 0.82 (6.9e-11) |
| | SI3-aEVP | -0.006 | 0.012 | 0.73 (1.16e-07) |
| P95 | SI3-BBM | -0.01 | 0.02 | 0.78 ( 3.64e-09) |
| | SI3-aEVP | -0.02 | 0.03 | 0.73 (9.7e-08) |
| P98 | SI3-BBM | -0.03 | 0.05 | 0.68 (1.24e-06) |
| | SI3-aEVP | -0.06 | 0.07 | 0.73 ( 9.4e-08) |

**Table 3.** Computational cost of 4 months of Arctic sea-ice simulation at 1/4°resolution with SI3 on the NANUK4 regional domain. BBM versus aEVP rheology, for both coupled (SI3-OCE, as performed for this study) and standalone (SI3-only) experiments.

| | **SI3-aEVP** | **SI3-BBM** | **BBM-related increase** |
|---|---|---|---|
| Coupled SI3 – OCE | 298 cpu h | 380 cpu h | +28% |
| Standalone SI3 | 139 cpu h | 223 cpu h | +60% |

https://doi.org/10.5194/gmd-2023-231
Preprint. Discussion started: 10 January 2024

Geoscientific Model Development
Discussions
Open Access
EGU

**Table A1.** Value of parameters used in the BBM simulation.

| Parameter | Definition | Value used |
|---|---|---|
| $\Delta x$ | local resolution (size) of the grid mesh (see Fig. 4) | ~ 14 km |
| $\nu$ | Poisson's ratio (Eq. 5) | 1/3 |
| $E_0$ | elasticity of undamaged sea-ice (Eq. 6) | 5.96 $10^8$ Pa |
| $\lambda_0$ | viscous relaxation time of undamaged sea-ice (Eq. 7) | $10^7$ s |
| $C$ | compaction parameter (Eq. 7, 6, 9) | -20 |
| $\alpha$ | damage parameter (Eq. 7) | 5 |
| $P_0$ | scaling parameter for ridging threshold (Eq. 9) | $10^4$ Pa |
| $h_0$ | reference ice thickness for ridging threshold (Eq. 9) | 1 m |
| $c$ | sea-ice cohesion (Eq. 14) | 5.8 $10^3$ Pa |
| $\mu$ | internal friction coefficient (Eq. 14) | 0.7 |
| $N$ | upper limit for compressive stress (Eq. 14) | 2.9 $10^7$ Pa |
| $\gamma_C$ | cross-nudging coefficient (Eq. 16) | 2 |
| $\Delta T$ | *big* time-step (advection & thermodynamics) | 720 s |
| $\Delta t$ | *small* time-step (BBM time-splitting) | 4 s |
| $N_s$ | $\equiv \Delta T/\Delta t$ | 180 |
| $k_{th}$ | healing constant for damage (Eq. 15) | 26 K s |
| $C_{Dw}$ | basal ice-water drag coefficient (Eq. B18) | 5.2 $10^{-3}$ |